Geologia USP
Série Científica

DOI: 10.11606/issn.2316-9095.v17-352
Revista do Instituto de Geociências - USP
Geol. USP, Sér. cient., São Paulo, v. 17, n. 2, p. 303-324, Junho 2017

The Proterozoic Guanhães banded iron formations, Southeastern border of the São Francisco Craton, Brazil: evidence of detrital contamination

As formações ferríferas bandadas proterozoicas de Guanhães, borda sudeste do Cráton São Francisco, Brasil: evidências de contaminação detrítica

Vitor Rodrigues Barrote[1], Carlos Alberto Rosiere[2], Vassily Khoury Rolim[2], João Orestes Schneider Santos[3], Neal Jesse Mcnaughton[4]
[1]Graduate Program, Instituto de Geociências, Universidade Federal de Minas Gerais - UFMG, 19/15 Tanunda Drive, Rivervale, 6.103, WA, Australia (vitorbarrote@hotmail.com)
[2]Instituto de Geociências, Universidade Federal de Minas Gerais - UFMG, Belo Horizonte, MG, BR (crosiere@gmail.com, vassily.rolim@gmail.com)
[3]Centre for Exploration Targeting, University of Western Australia, Perth, WA, Australia (orestes.santos@bigpond.com)
[4]John de Laeter Centre for Isotope Research, Curtin University, Perth, WA, Australia (n.mcnaughton@curtin.edu.au)

Received on December 11th, 2015; accepted on April 28th, 2017

Abstract
The Guanhães banded iron formation (BIF) bearing succession occurs as tectonic slices, juxtaposed to Archean TTG granite-gneissic basement rock, developed during the Neoproterozoic-Cambrian Brasiliano collage. The succession has a maximum depositional age of ~2.18 Ga, from detrital zircons in quartzite, and consists of quartzites, schists, BIFs, gneiss and amphibolite, all metamorphosed under amphibolite facies conditions. The Guanhães BIF shows HREE enrichment and consistent positive Eu anomaly (PAAS-normalized REE+Y). Two types of contamination were observed in the samples. The first is contamination by an exotic detrital component, which resulted in low Y/Ho (< 30) and Pr/Yb (SN) ratios. Evidence of such contamination, combined with inferred stratigraphic stacking data, indicates that the Guanhães BIFs were deposited on a shallow marine environment. The second type of contamination resulted in higher Eu-anomalies, positive Ce-anomalies, and higher REE+Y concentrations, possibly due to the interaction between later magmatic fluids and the Guanhães BIF. A strong Cambrian event is recorded in zircon age data. The uncontaminated samples display REE+Y distribution similar to other Precambrian BIFs, particularly those from the Morro-Escuro Sequence and the Serra da Serpentina Group, without true Ce-anomalies and Y/Ho close to seawater values (45). Geochronological and geochemical data presented in this paper strongly suggest a correlation between the Guanhães supracrustal succession and the Serra da Serpentina and Serra de São José Groups.

Keywords: Banded Iron Formation; Guanhães; Geochronology; Geochemistry.

Resumo
A sequência supracrustal Guanhães, portadora de formações ferríferas bandadas (BIFs), ocorre como fatias tectônicas superpostas ao embasamento de terrenos granito-gnáissicos do tipo TTG de idade Arqueana, desenvolvidas no limite entre o período Proterozoico e o Paleozoico, durante a colagem Brasiliana. A idade máxima de deposição da sucessão é de ~2,18 Ga e foi determinada por datação de zircões detríticos em quartzitos. Além de quartzitos, a sucessão é composta por xistos, BIFs, gnaisses e anfibolitos, todos metamorfisados em condições de fácies anfibolito. A análise dos Elementos Terras Raras + Y (ETR+Y), normalizados ao PASS, para as BIFs de Guanhães, mostra enriquecimento em ETR pesados e anomalia positiva de Eu. Dois tipos de contaminação foram observados nas amostras. O primeiro é uma contaminação detrítica que resultou em baixos valores de Y/Ho (< 30) e Pr/Yb (SN). As evidências de contaminação desse tipo, combinadas à análise do empilhamento estratigráfico do pacote de rochas supracrustais, indicam que as BIFs de Guanhães foram depositadas em ambiente marinho raso. Um evento Cambriano expressivo está presente nos dados relativos à datação de zircões. O segundo tipo de contaminação resultou em maiores valores de anomalia de Eu, anomalia positiva de Ce e maiores concentrações de ETR, possivelmente devido à interação entre fluidos magmáticos posteriores e as BIFs de Guanhães. As amostras sem contaminação mostram distribuição de ETR semelhante a outras BIFs Pré-cambrianas, particularmente às BIFs da Sequência do Morro Escuro e do Grupo Serra da Serpentina, com ausência de anomalia verdadeira de Ce e Y/Ho próximo aos valores da água do mar (45). Os dados geocronológicos e geoquímicos apresentados neste artigo sugerem correlação entre a sucessão supracrustal de Guanhães (GSSu) e os Grupos Serra da Serpentina e Serra de São José.

Palavras-chave: Formações Ferríferas Bandadas; Guanhães; Geocronologia; Geoquímica.

INTRODUCTION

The Guanhães Group (Grossi-Sad, 1997) contains several small, discontinuously distributed, and highly deformed tectonic slices of Banded Iron Formation (BIF) that are associated with a metasiliciclastic succession. The metasedimentary succession remnants are distributed over an area of approximately 2,500 km^2 around the Guanhães township, about 150 km Northeast of the world known Quadrilátero Ferrífero mining district, in Minas Gerais, Brazil (Figure 1). The existence of a BIF in this region has long been known, with references as old as 1833 (Grossi-Sad, 1997), but geological studies in the area, including stratigraphy, structural geology and geochemistry, are limited to the regional scale (Grossi-Sad et al., 1989, 1990a; Grossi-Sad, 1997; Pedrosa-Soares et al., 1994). Only Grossi-Sad et al. (1990b), based on geochemical data, classified the Guanhães BIFs as of Algoma-type and estimated an Archean age for the succession.

This study focusses on BIFs from the Jambreiro quarry, which is located in the central region of known ore bodies where outcrops are few and discontinuous. The target area represents a typical and relatively well-exposed occurrence of the supracrustal succession, with several fresh, unaltered core drill samples that makes it suitable for chemical characterization of the Guanhães BIF, as well as for a first approach to the interpretation of its sedimentary environment.

The present paper discusses the geochemistry and geochronology of the Guanhães BIFs in the light of modern analytical techniques, such as sensitive high-resolution ion microprobe (SHRIMP) zircon dating and inductively coupled plasma mass spectrometry (ICP-MS) geochemistry. This contribution provides valuable information to explore iron in such region, and seeks to understand the depositional basin characteristics, the nature of postdepositional processes they were subjected to, and the relationship with the surrounding areas and other metasedimentary successions. These interpretations are complemented by detrital zircon dating from quartzite layers closely associated with the BIF.

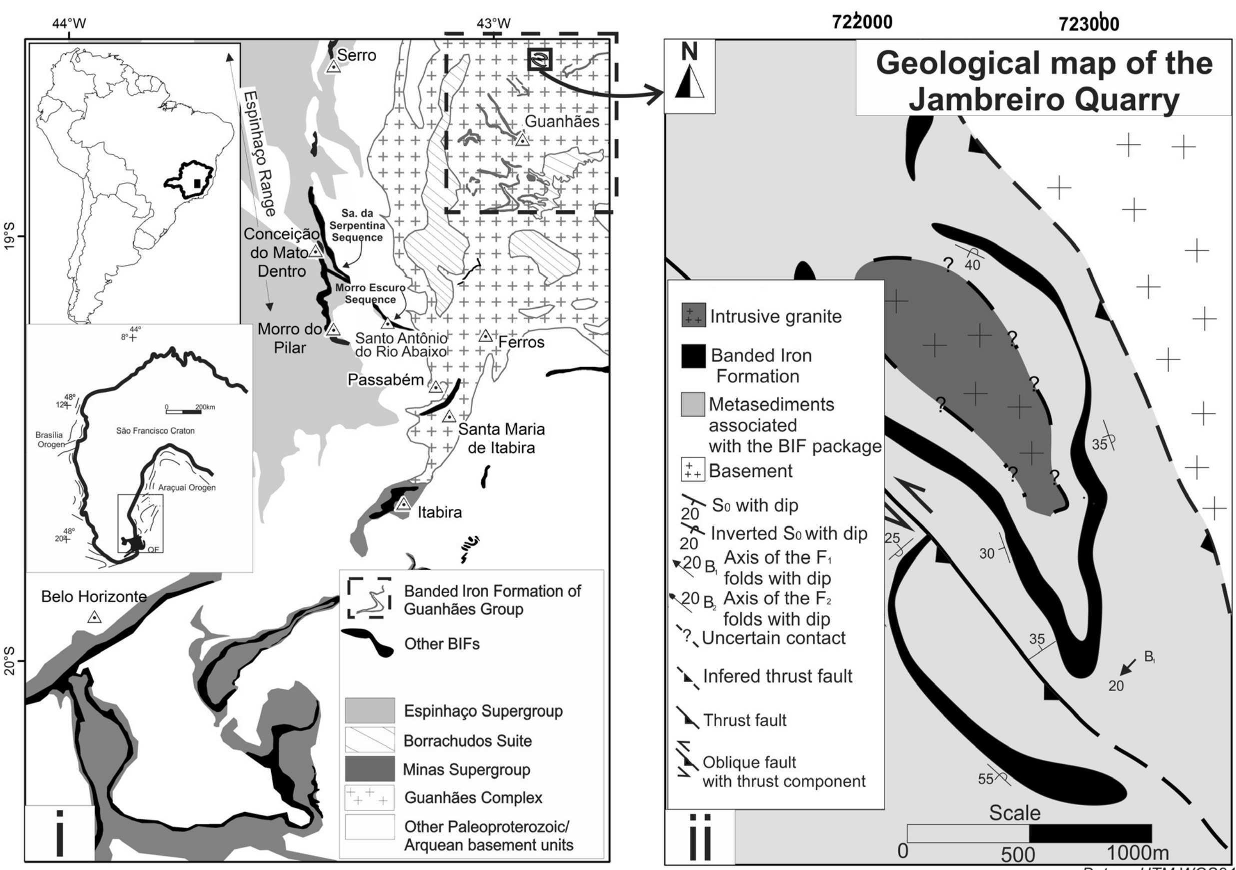

Figure 1. (A) Regional geological map showing the location of the Guanhães Group's Banded Iron Formation (BIFs) and distribution of others BIF-bearing successions nearby in the Quadrilátero Ferrífero region in Southeast Brazil (based on Grossi-Sad, 1997; Pedrosa-Soares et al., 1994). The entire region is located on the limit between the São Francisco Craton and the Araçuaí Orogen (based on Alkmin et al., 2006). (B) Geological map of the Jambreiro quarry (from Barrote, 2016).

GEOLOGICAL SETTING

The Guanhães Group (Grossi-Sad, 1997) represents a BIF-bearing supracrustal sequence that occurs in the East of the Espinhaço Range (Figure 1), in highly deformed terranes, named the Guanhães Basement Block (Alkmim et al., 2006).

It is believed the Guanhães Basement Block is the product of crustal agglutination of Archean blocks that occurred during the Rhyacian orogenesis, affecting the Paleoproterozoic units approximately between 2.2 and 2.0 Ga (Noce et al., 2007). According to Alkmim et al. (2006), the block would have acted as a structural high during the Araçuaí Orogen already at the early stages of the orogeny, during the rifting phase (~875 Ma on Silva et al., 2002). The Neoproterozoic Araçuaí orogeny is one of many Brasiliano/Pan-African orogens that were developed in the assembly of West Gondwana (Pedrosa-Soares and Noce, 1998; Pedrosa-Soares and Wiedemann-Leonardos, 2000; Pedrosa-Soares et al., 2001, 2007).

The Araçuaí Orogen consists of several distinct structural domains, which differ from one another in terms of style, orientation, deformation history, and shear sense. According to Alkmim et al. (2006), following the criteria adopted by Almeida et al. (1981), the Guanhães Complex, including the supracrustal BIF-bearing sequence, would be part of the basement to the Araçuaí orogeny that includes all units older than 1.8 Ga.

The Guanhães' BIFs are part of the Guanhães Group, which is a succession of metasedimentary rocks superposed on Archean Tonalite-Trondhjemite-Granodiorite (TTG) granite-gneissic basement (Pedrosa-Soares et al., 1994; Grossi-Sad, 1997; Silva et al., 2002). The Guanhães Group consists of schists, quartzites and paragneisses interpreted by Grossi-Sad et al. (1989, 1990a, 1990b) and Grossi-Sad (1997) as having metavolcano-sedimentary origin. Several authors place such group as part of the Archean Guanhães Complex, without distinctions of crystalline basement rocks from the supracrustal succession (Pedrosa-Soares et al., 1994; Dussin et al., 2000; Silva et al., 2002; Noce et al., 2007).

In the studied area, the metasedimentary succession directly associated with the Guanhães BIFs (Figure 2) consists, from bottom to top, of:

- a lower quartzitic unit up to 50 m thick comprising mainly medium to coarse grain quartzites with saccharoidal texture of variable composition (pure, sericitic, arkosic and iron-rich), intercalated with gneiss and schist;
- the BIF (itabirite), which also displays a medium to fine grained saccharoidal texture. The iron oxide mineralogy comprises mainly hematite with variable morphologic characteristics (lamellar/specularite, granular and martite) and magnetite;
- an upper quartzitic unit that is very similar to the basal unit. The main difference here is the presence of garnet-rich amphibolite layers, which are close to the contact with the underlying BIF unit.

Several intrusive granites and associated pegmatites crosscut the metasedimentary rocks of the Guanhães Group. The granites show similar mineralogy, but they can be either massive and isotropic or locally overprinted by a S_1 foliation (Barrote, 2016).

The supracrustal rocks display mineral assemblages typical of high amphibolite facies (Grossi-Sad, 1997; Fernandes et al., 2000; Fernandes, 2001; Dussin et al., 2000). The metamorphic imprint was dated as 519-507 Ma (Noce et al., 2007), which indicates that the Guanhães block exposes rocks of a deeper crustal level, which is probably uplifted during the final stages of the Neoproterozoic-Cambrian Brasiliano collage (Knauer and Grossi-Sad, 1997).

METHODOLOGY

Geochemistry

Seventeen fresh BIF samples were collected in different stratigraphic positions from 11 drill cores from the Jambreiro Iron Ore Project of Centaurus Metals Ltd. Eight of them were selected for thin sections and petrographic examination. For the geochemical analysis, the samples were pulverized with the use of a hand-held drill machine containing a small diamond disc (1 cm in diameter).The silica- and iron-rich bands of the BIF samples were not analyzed separately.

The geochemical analyses were accomplished at the Acme Analytical Laboratories, in Vancouver, Canada. Samples were analyzed with the LF202 (AQ200 add on – LF302 + LF100-EXT) package of Acme Labs (Acme, 2014). The inductively coupled plasma emission spectrometry (ICP-ES) is

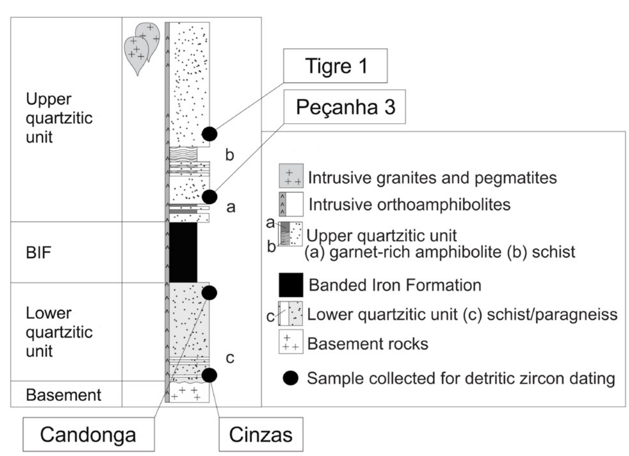

Figure 2. Stratigraphic succession of the Guanhães supracrustal succession showing stratigraphic location of samples selected for detrital zircon dating.

the chosen method used for major oxide elements and the inductively coupled plasma mass spectroscopy (ICP-MS) is applied for trace elements (including REE), following a dissolution by hot Aqua Regia digestion or lithium borate fusion (Acme, 2014). Precision and accuracy of the analyses were monitored through Acme Labs internal procedures.

Concentrations of rare earth elements plus yttrium (REE+Y) in the BIF samples were normalized to Post-Archaean Average Shale (PAAS) of McLennan (1989) and to the chondrite of Taylor and McLennan (1985).

Geochronology

U-Pb sensitive high-resolution ion microprobe (SHRIMP) determinations were performed on detrital zircon crystals of four samples, from the upper and lower quartzitic units, and investigated using SHRIMP at the John de Laeter Center for Isotopic Research from the Curtin University in Perth, Western Australia. The samples were processed with conventional crushing, grinding and screening in the LOPAG-DEGEO laboratory at Universidade Federal de Ouro Preto. After the concentration, the four samples were sieved and washed to remove fine-grained material (clay and silt size). The 60-250 mesh fraction was treated with heavy liquid (TBE, tetrabromoethane) to remove light minerals. A Frantz LB1 magnetic separator was used to separate the less magnetic fraction where zircon is concentrated. Zircon was handpicked and organized in two epoxy mounts (UWA 13-22 and UWA 13-23), which were polished and coated with carbon for the Scanning Electron Microscope (SEM) study. Backscattered electron images (BSE) were taken using a JEOL6400 SEM at the Centre for Microscopy, Characterisation and Analysis of the University of Western Australia. Imaging of the zircon is critical for identifying internal features, like core and rims, and to avoid areas with high common lead content (inclusions, fractures, and metamict areas). Epoxy mounts were coated with gold for SHRIMP analyses. Most SHRIMP analytical spots were in the diameter range of 20-30 μm; however, in the presence of alteration haloes due to hydrothermal recrystallization, a spot size of only 10 μm was applied and greater spatial resolution was required. Four scans were used for each spot analysis of detrital zircon and six scans during the analyses of hydrothermal areas. The following masses were analyzed for zircon: $^{196}Zr_2O$ ^{204}Pb, background, ^{206}Pb, ^{207}Pb, ^{208}Pb, ^{238}U, ^{248}ThO, and ^{254}UO. The zircon standard CZ3 (561.5 Ma, 551 ppm U) was used for U/Pb and U-content standard, and NBS611 was applied to identify the position of the mass peak ^{204}Pb. OGC-1 zircon was used as a $^{207}Pb/^{206}Pb$ monitor. All data on detrital zircon with common lead correction greater than ~0.5% were detected during the first scan, and then the analysis was aborted. Uncertainties of individual ages are quoted at 1σ level, whereas the ages plotted are calculated at 2σ levels (about 95% confidence). SHRIMP data were reduced using SQUID software (Ludwig, 2001) and plots were prepared using ISOPLOT/Ex (Ludwig, 2003). The main lead loss is not modern, but it occurred at about 500 Ma and $^{207}Pb/^{206}Pb$ ages are presented for both modern and Cambrian Pb-losses.

PETROGRAPHY

The mineralogical composition of the Guanhães BIFs varies slightly in both mineral content and proportions. The composition is in average: quartz (40-50%); iron oxides (20-35%); amphibole (5-20%); carbonates + chlorite (1-10%); and accessories – such as epidote, muscovite and zircon (< 2.5%). The quartz grains are irregularly shaped and exhibit deformational features, such as undulose extinction. Quartz and magnetite are locally intermixed with a coarser granular fabric that partially obliterates the banded structure. Otherwise, the BIFs usually display a regular banding in meso (cm) to microscale (mm). The contact between "iron-rich" and "iron-poor" microbands is usually sharp, but more diffuse transitions within the "iron-poor" laminae are observed, which probably reflect the primary BIF-features (Figures 3A and 3B).

Iron-rich laminae are largely composed of hematite, but they show distinct textural features such as specular and granular (Figures 4A and 4B, respectively). Magnetite tends to occur as inclusion-free sub-hedral to euhedral, thin to medium-grained crystals (0.4 to 1.0 mm; Figure 4B). The intergrowth and genetic relation between magnetite and hematite along the original primary bands of the BIFs is not clear, but the occurrence of martite with relicts of magnetite indicates that magnetite predated at least one generation

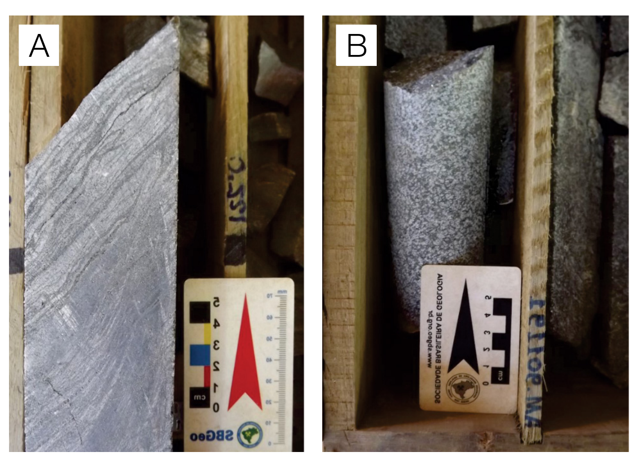

Figure 3. (A) Drill core showing microbanded Banded Iron Formation samples, with intrafolial folds. (B) Drill core showing coarse-grained iron formation with obliterated banded structure.

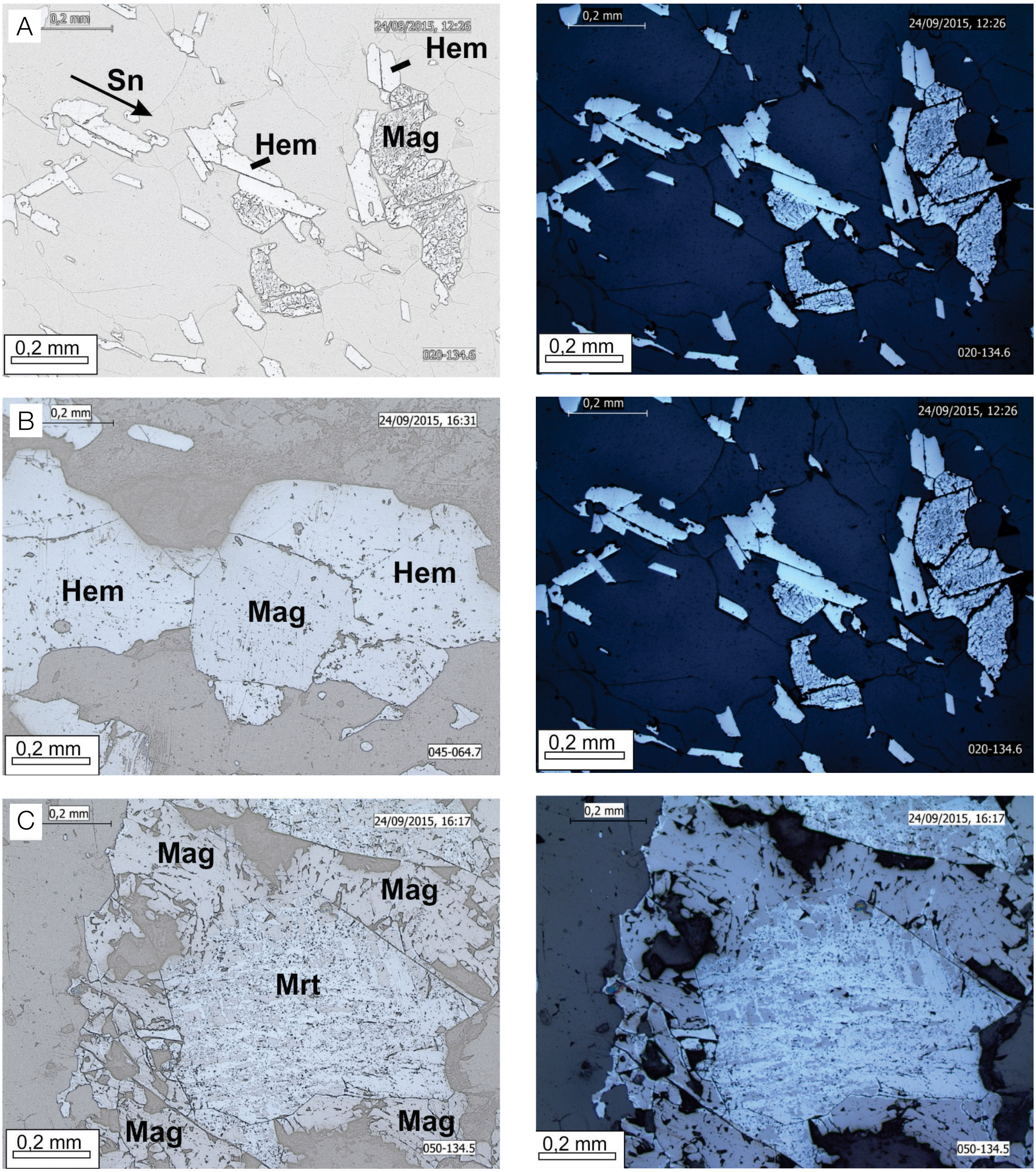

Mag: magnetite; Hem: hematite; Mrt: martite.

Figure 4. Schematic drawing (on the left) and correlated microphotography (on the right) of the Guanhães Banded Iron Formation (BIF) under reflected light, focused on texture and structure of the iron oxides. (A) Two generations of specular hematite. The first generation is distributed into the iron-rich bands of the BIF and the second generation is oriented concordant to the foliation (Sn). Sub-hedral crystals of magnetite are distributed through the iron-rich band and are cut by the second generation of specularite. (B) Euhedral magnetite and granular hematite in an iron-rich band. (C) Sub-hedral martite (hematite pseudomorph of magnetite) with residues of magnetite and sub-hedral magnetite crystals within an iron-rich band.

of hematite (Figure 4C). A younger generation of oriented specularite superposes the granular-textured iron oxides on iron rich bands (Figure 4A).

Iron poor layers are mainly composed of quartz with polygonal contacts, wavy extinction and straight to irregular grain boundaries (Figure 5A). There are two varieties of amphiboles in the Guanhães BIFs: the first is colorless syn-deformational tremolite (Figure 5B), with crystals presenting the same orientation as the younger specularite; the second is associated with hornblende that also occurs preferably as random crystals in the iron-rich bands and is strongly pleochroic (pale green, dark green to deep bluish green) that indicates high iron content (Figure 5C).

Iron rich and quartz layers are occasionally interlayered with thin (1-2 mm) white to pale brown (Figures 5C and 5D). The samples can be separated into two groups, according to the presence or absence of carbonates. Samples 051-115.2, 050-134.5, 051-123.0, 020-113.3, 027-127.7 and 052-133.5 contain carbonate, as indicated in Table 1.

GEOCHRONOLOGY

The age of detrital zircons provides robust documentation of the source region of siliciclastic sediments. Vermeesch (2004) states that dating a large number of detrital zircon crystals is required in order to detect a source area that represents 5% of

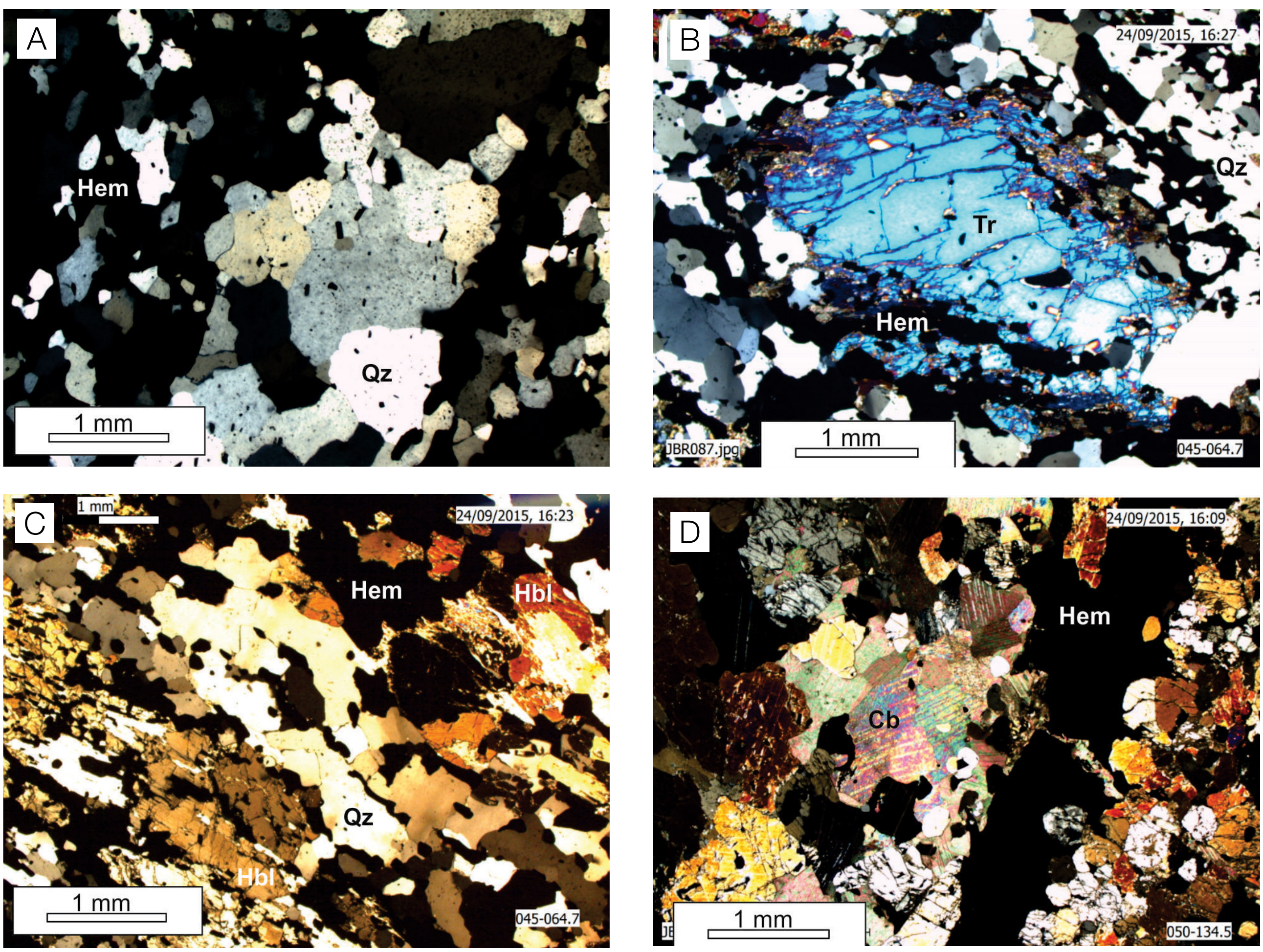

Qz: quartz; Tr: tremolite; Hbl: hornblende; Cb: carbonate.

Figure 5. Microphotography of the Guanhães Banded Iron Formation (BIF) under transmitted light, taken with crossed polars. (A) Iron-rich band with predominance of hematite and silica-rich band with predominance of quartz, with polygonal contacts, wavy extinction and straight to irregular grain boundaries. (B) Tremolite crystal in an iron-rich band, syn-formational to the specular hematite (i.e. syn-deformational). (C) Iron-rich band with predominance of hematite and hornblende. The hornblende is locally altered to carbonate. Silica-rich bands with predominance of oriented quartz and occurrence of carbonate. (D) Euhedral to sub-hedral crystals of non-oriented carbonate on a silica-rich band. The iron-rich band is predominantly composed of hematite and hornblende (not shown).

the population (95% confidence interval). However, several authors consider that a much smaller number of grains must be analyzed to detect major sources, while minor sources that contribute 10% or less to the filling of the basins may remain undetected (Hartmann et al., 2006; Silveira-Braga et al., 2015; Rolim et al., 2016).

In this study, we investigated from 19 (Peçanha3) to > 30 (Cinzas and Tigre1) zircon crystal grains in each sample in order to identify the main populations and ages from the source rocks. The maximum depositional age for the quartzitic units associated with the BIFs of the Guanhães supracrustal succession (SSGu) was determined based on the youngest population of detrital zircon grains.

Four samples were selected from the upper and lower quartzitic units and zircons; then they were separated and investigated using SHRIMP (Appendix A). In the four samples, the grains are sub-rounded to rounded (Figures 6A, 6B and 6C), although some prismatic crystals were also observed (Figures 6A and 6B). All samples have several grains that show compositional rims, which are visualized through backscattered electron (BSE) images (Figures 6D, 6E and 6F). Some rims display diffuse contacts with core regions and are atypical of igneous growth. They are coupled with the presence of concordant Cambrian ages (~500 Ma) in all samples (Figures 6E and F; Appendix A), which complicates the interpretation of detrital age data.

All samples have some zircon analyses at ~500 Ma and, when combined, yield a $^{207}Pb/^{206}Pb$ age of 519 ± 14 Ma (n = 18; MSWD = 0.75). These analyses came from disturbed areas within detrital zircons and have significantly higher U-content. This would have resulted in enhanced radiation damage and metamictization, leading to a preferential replacement during a later event. Furthermore, all of the ~500 Ma analyses have a distinctive low Th/U (i.e. 16 of 18 analyses have Th/U < 0.05). The nature and extent of this disturbance is currently unclear and awaits further analysis.

One consequence of this disturbance is Pb-loss within detrital zircons at this time, and the production of Pb-loss chords towards ~500 Ma on Concordia plots. Accordingly, data in Appendix A have been calculated for both current and Cambrian Pb-loss, which is discussed further below. Single ages that do not overlap other analyses (within error) are not considered reliable indicators of a detrital age due to possible Pb-loss.

LOWER QUARTZITIC UNIT

Of the 32 analyzed grains, 2 are Cambrian and 16 are within the 10% concordance level. In this case, the data for recent Pb-loss are applicable. The youngest ages obtained from the sample CINZAS is ~2.71 Ga (n = 2), which points to source

Table 1. Composition of the major elements from the Guanhães BIF at the Jambreiro quarry.

XRF	SiO_2	TiO_2	Al_2O_3	FeOt	MnO	MgO	CaO	Na_2O	K_2O	P_2O_5	with Cb
Sample											
008-046.1	45.17	<0.01	0.2	54.4	0.02	<0.01	0.02	<0.01	<0.01	0.05	
020-134.6	47.53	0.04	1	49.71	0.04	0.13	0.13	0.01	0.02	0.04	
037-055.0	52.43	0.02	1.02	45.76	0.02	<0.01	0.02	<0.01	0.02	<0.01	
039-040.0	51.97	0.03	1.37	45.74	0.05	<0.01	0.01	<0.01	0.02	<0.01	
040-051.2	48.83	0.03	0.36	50.42	0.01	<0.01	<0.01	<0.01	<0.01	<0.01	
042-028.0	54.55	0.04	1.21	43.53	0.03	<0.01	0.01	<0.01	0.02	<0.01	
045-045.9	51.66	0.02	0.41	47.18	0.02	<0.01	0.02	<0.01	<0.01	<0.01	
045-064.7	44.15	0.06	0.69	45.37	0.21	4.51	4.13	0.06	<0.01	0.13	
051-115.2	8.78	0.41	2.01	49.93	0.32	8.6	13.42	0.02	0.16	0.12	yes
050-134.5	37.48	0.03	0.53	49.93	0.21	4.52	6	0.05	0.01	0.06	yes
051-123.0	32.11	0.03	0.44	39.76	0.43	9.83	13.39	0.06	<0.01	0.09	yes
020-113.3	52.92	0.5	0.44	46.05	0.07	<0.01	0.02	<0.01	<0.01	0.05	yes
027-127.7	12.78	0.5	0.73	47.11	0.43	6.81	17.97	0.01	0.03	0.09	yes
052-133.5	53.55	0.3	0.38	43.47	0.04	0.42	1.08	<0.01	<0.01	0.12	yes
052-152.7	51.75	1.1	0.95	44.14	0.09	0.73	1.14	0.02	0.1	0.15	
050-112.5	53.34	0.5	0.35	45.71	0.03	0.02	0.16	<0.01	<0.01	0.12	
051-112.4	49.32	0.4	0.44	49.37	0.05	0.13	0.22	<0.01	0.03	0.17	

*samples that have Carbonate (Cb) are indicated ** strikethrough samples are weathered and not considered in the discussion

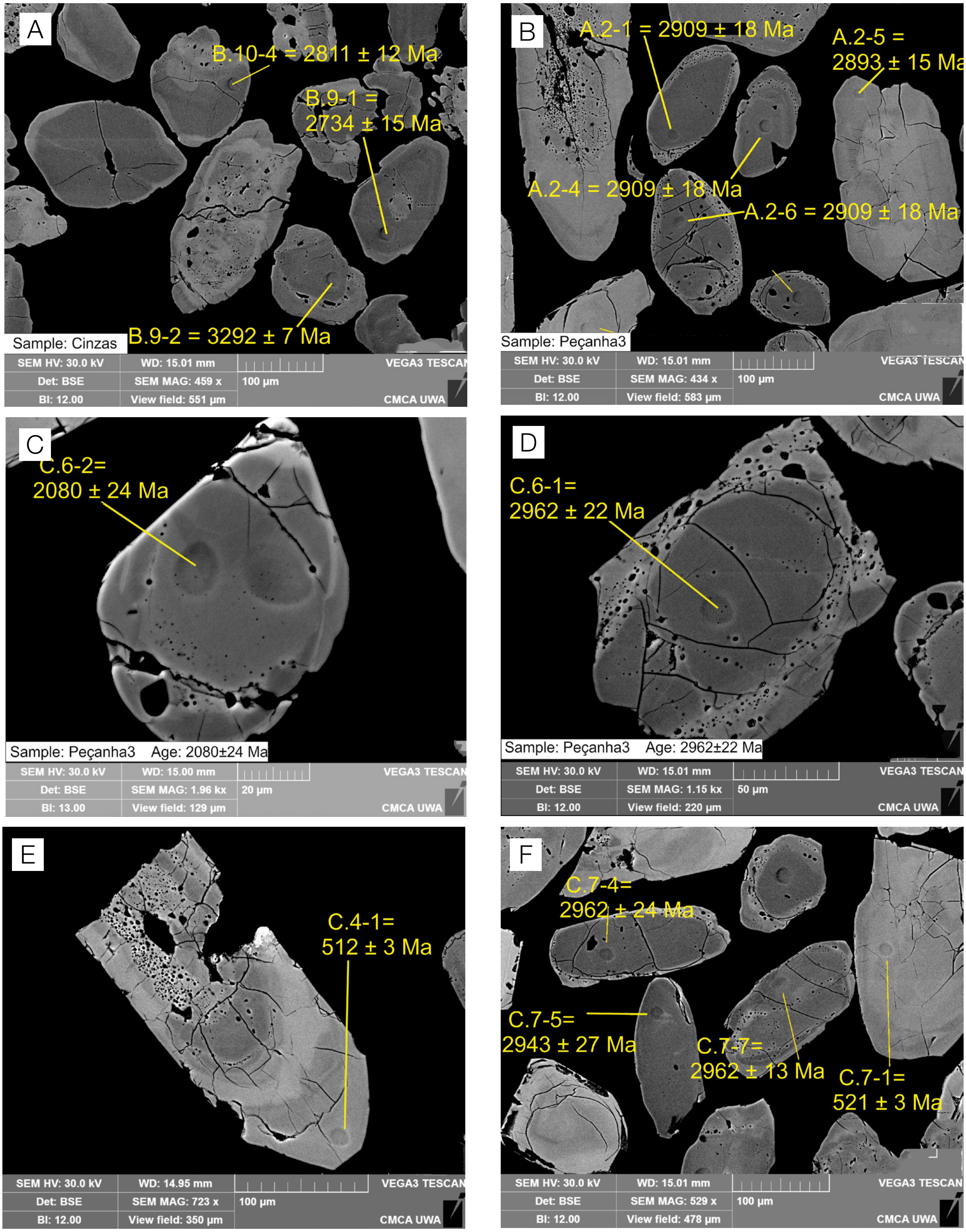

Figure 6. Backscattered electron (BSE) image of selected detrital zircon grains from samples Cinzas (A) and Peçanha 3 (B). (C) and (D) Small scale BSE images of a couple of zircon grains from the sample Peçanha 3, of Rhyacian and Archean age, respectively. (E) Small scale BSE image of a zircon grain from the sample Cinzas with analyses at ~500 Ma in an area that has significantly higher U-content within the detrital zircon. (F) BSE images of a couple of zircon grains of Archean age from the sample Cinzas and a zircon grain with analyses at ~500 Ma, the difference in U content is evidenced by the brightness differences between grains.

rocks of Archean age. For the 16 data which are > 10% discordant and for which Cambrian Pb-loss is applicable, a single analysis of ~2.66 Ga is of uncertain validity as a detrital zircon age, therefore 2.71 Ga are taken as the maximum depositional age. 34 analyses were performed on zircon grains from the lower quartzitic unit (CANDONGA). Five of the 34 analyses were Cambrian. Omitted single analyses at ~1.70 and ~2.68 Ga were of uncertain veracity. The youngest grouping (of two analyses) is ~2.77 Ga, reflecting an Archean source.

UPPER QUARTZITIC UNIT

The Tigre1 sample from the upper quartzitic unit at the Jambreiro Quarry shows a different pattern of zircon ages when compared to the lower unit. 34 analyses include 4 Cambrian and 1 spectrum of Archean-Proterozoic ages, and 11 of them define the youngest population at ~2.18 Ga, which is considered the maximum age of deposition.

Archean grains also dominate the other sample from the upper quartzitic unit (Peçanha3). Among the 26 detrital zircon analyses, 7 are Cambrian and the youngest population (of 2 grains) is ~2.1 Ga, which is similar to Tigre1.

Excluding Cambrian analyses, the detrital zircon age data for the combined SSGu dataset are shown in Figure 7. There is strong input of Archean grains (about 80% of the detrital material) with ages from ~2.7 to ~3.3 Ga followed by about 20% of Paleoproterozoic input (~2.18 Ga).

GEOCHEMISTRY

Major and trace elements

Major and selected trace element content in the Guanhães BIF obtained from the Jambreiro quarry are presented in Tables 1 and 2, respectively. Chondrite and PAAS-normalized REY-diagrams (REE+Y) are shown in Figures 8A and 8B.

The SiO_2 and Fe_2O_3 content range from 8.78 to 54.55% and from 39.76 to 54.40%, respectively. The samples display relatively low content in Al_2O_3, TiO_2, Zr, Nb, Sc, Cr, V, and Ni.

Figure 8 shows that, with the exception of two samples ("042-028.0" and "039-040.0"), the REE+Y spectra of the other samples are consistent. Samples 042-028.0 and 039-040.0 show an anomalous enrichment in LREE

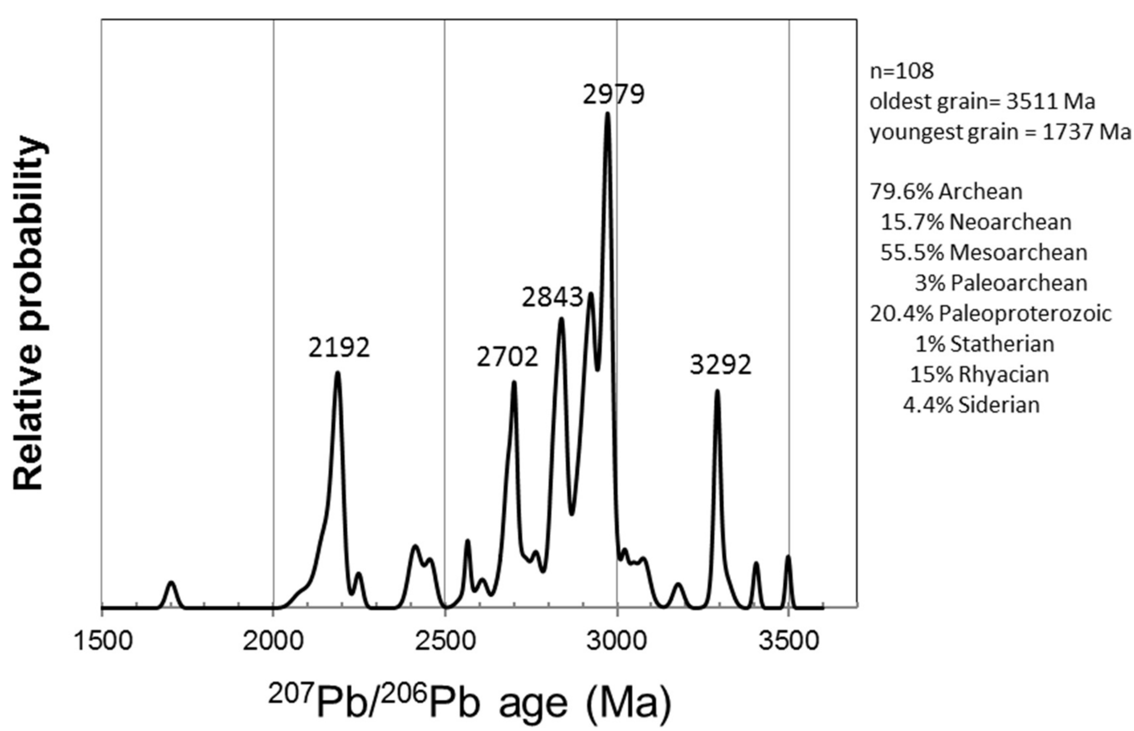

Figure 7. Age probability diagram for the combined age data obtained from detrital zircon grains from the SSGu in the Guanhães region. Major populations are at the ages of 2192, 2702, 2843 and 2979 Ma (main population), and 3292 Ma. There is a single 1737 Ma analysis that does not overlap other analyses (within error).

Table 2. Selected trace elements composition from the Guanhães BIF at the Jambreiro quarry in ppm.

Sample	020-134.6	037-055.0	039-040.0	040-051.2	042-028.0	045-045.9	045-064.7	051-115.2	050-134.5	051-123.0	020-113.3	008-046.1	027-127.7	052-133.5	052-152.7	050-112.5	051-112.4
Sc	1	1	1	<1.00	1	<1.00	<1.00	4	<1.00	<1.00	1	2	1	<1.00	1	<1.00	<1.00
Cr2O3	0.11	<0.002	<0.002	<0.002	<0.002	<0.002	<0.002	0.01	0.01	<0.002	0.01	<0.002	0.01	<0.002	0.01	0.01	0.01
Rb	1.3	0.6	0.5	<0.1	0.5	<0.1	<0.1	4.3	0.3	<0.1	<0.1	0.3	1.1	0.2	2.8	0.1	0.5
Sr	2.7	10.2	4.4	4.4	6.7	2.2	11.7	86.1	14.1	34.1	0.38	0.69	0.9	0.29	1.05	0.48	0.69
Y	4.1	6.9	4.2	1.5	3.7	2.5	10.2	10.8	6.9	10.3	3.8	2.6	11	2.9	7.6	4.5	9.4
Zr	14.8	9.4	11.6	10.4	13.3	10.5	70.8	70.5	26.4	19.3	9.2	9	11.8	8.2	22	7.4	10
Hf	0.2	0.2	0.3	0.2	0.4	0.1	1.7	2	0.6	0.4	0.3	0.1	0.2	0.2	0.6	0.1	0.2
Pb	0.9	0.4	1.6	0.9	0.7	1	5.5	4.5	1.5	2.3	0.8	0.3	5.3	0.5	1.8	0.5	0.4
Th	1.1	0.4	0.6	0.7	0.7	0.4	13.6	1.3	0.6	0.5	0.02	0.01	0.04	0.01	0.03	0.01	0.02
U	2	1.4	0.7	0.5	0.6	0.8	1.6	2.4	2.5	3.6	1	0.8	4.3	3	1.1	1.6	2.1
La	3	5.7	14.9	3.6	19.9	2.7	4.8	4.2	5.5	2.8	3	5	7.3	3.2	7	2.3	6.2
Ce	6.6	9.9	35.4	6.8	33.5	5.1	10.6	6.7	9.5	5.6	5.6	7.8	10.8	5.5	15.9	5.8	11.5
Pr	0.73	1.31	2.52	0.65	5.09	0.56	1.19	0.86	0.96	0.72	0.5	0.89	1.26	0.56	1.28	0.53	1.06
Nd	2.4	6	7.2	2.1	17.1	2.5	4.8	3.8	3.3	3.1	1.8	3.6	4.8	2.5	4.5	2.3	4.1
Sm	0.55	1.54	0.99	0.57	2.37	0.42	1.09	0.69	0.61	0.83	<0.05	1	<0.05	<0.05	<0.05	<0.05	<0.05
Eu	0.2	0.59	0.32	0.14	0.64	0.17	0.52	0.31	0.29	0.34	0.14	0.3	0.38	0.11	0.43	0.24	0.38
Gd	0.6	2.07	0.93	0.46	1.38	0.39	1.3	1.02	0.71	1.02	0.48	0.76	1.13	0.44	1.05	0.56	0.98
Tb	0.09	0.32	0.12	0.06	0.19	0.07	0.23	0.16	0.11	0.16	0.07	0.11	0.17	0.06	0.14	0.08	0.14
Dy	0.62	1.68	0.58	0.36	0.89	0.37	1.48	1.09	0.68	1.09	0.46	0.55	1.09	0.4	0.85	0.5	1.13
Ho	0.15	0.3	0.1	0.06	0.15	0.1	0.29	0.3	0.16	0.24	0.08	0.09	0.28	0.07	0.2	0.13	0.26
Er	0.44	0.66	0.38	0.23	0.41	0.32	0.98	0.83	0.52	0.76	0.27	0.21	0.81	0.24	0.64	0.37	0.7
Tm	0.06	0.09	0.06	0.02	0.07	0.04	0.15	0.14	0.06	0.12	0.05	0.02	0.12	0.04	0.11	0.06	0.11
Yb	0.48	0.57	0.47	0.2	0.46	0.33	1.13	0.94	0.52	0.75	0.31	0.16	0.81	0.24	0.68	0.37	0.76
Lu	0.08	0.08	0.06	0.04	0.06	0.04	0.19	0.17	0.07	0.14	0.04	0.01	0.13	0.03	0.12	0.05	0.13
Y/Ho	27.33	23	42	25	24.67	25	35.17	36	43.13	42.92	47.5	28.89	39.29	41.43	38	34.62	36.15
Ce/Ce*(SN)	1.03	0.84	1.32	1.02	0.77	0.96	1.02	0.81	0.94	0.91	1.04	0.85	0.81	0.94	1.22	1.21	1.02
Pr/Pr*(SN)	1.99	2.39	1.28	1.72	2.74	1.98	0.98	0.99	1	1.01	0.92	0.99	1.03	0.89	0.87	0.85	0.9
Eu/Eu*(SN)	1.74	1.66		1.35		1.93	2.06	1.86	2.19	1.84	1.42	1.64	2.6	1.17	2.05	1.32	1.81

when normalized to the PAAS and a very pronounced LREE enrichment when chondrite-normalized (Figure 8). Those samples are considered affected by weathering, causing the accumulation of LREE in clay and hydroxide particles, and are not considered in the discussion of Proterozoic compositions. The chondrite-normalized (Taylor and McLennan, 1985) REY-diagram (Figure 8A) for the Guanhães BIF indicates a pronounced LREE enrichment in relation to HREE ($Pr/Yb_{[SN]}$ = 0.61 in average) as illustrated in Figure 8. The Eu anomaly is, in general, slightly positive with an average of 1.03 (Eu/Eu*(CN) = (Eu (CN)/0.5Sm (CN) + 0.5Gd (CN)) = 0.44-1.34).

As normalized to the PAAS (McLennan, 1989), the REY diagram (Figure 8B) shows the typical HREE enrichment as to LREE [(Pr/Yb) (SN) = 0.86 on average]. The Eu anomaly is generally positive with an average of 1.59, close to the value of 1.5 proposed by Planavsky et al. (2010) that characterizes the late Proterozoic iron formations [Eu/Eu* (SN) = Eu (SN)/ (0.66 Sm (SN) + 0.33 Tb (SN)) = 0.84-1.96].

Element correlations

The Guanhães BIF samples display a positive correlation between the lithophile elements Hf and Zr (Figure 9). However, they lack some correlation between Th and Zr.

The samples can be divided into two major groups according to their Y/Ho (Figure 10). The first group comprises five samples with Y/Ho under 30. The rest of the samples can be further grouped based on the presence or absence of carbonate. Carbonate-rich BIF samples have higher Y/Ho, ranging from around 40 to 47, whereas samples that do not contain carbonate show Y/Ho close to 35.

Samples with low Y/Ho do not present any correlation neither between the LREE/HREE ratio and Y/Ho (Figure 10A) nor between the Eu/Eu*(SN) and Y/Ho (Figure 10B). The remaining samples show a slightly positive correlation between the LREE/HREE ratio and Y/Ho (Figure 10A) and a weak negative correlation between Eu/Eu*(SN) and Y/Ho (Figure 10B). BIFs without carbonate present slightly higher Eu anomalies (Figure 10B).

Ce-anomaly

The Ce anomaly is recognized as one of the fundamental features of lanthanide geochemistry (Taylor and McLennan, 1985). Due to its sensitivity to redox state of the environment, Ce is a prime proxy for ocean-atmosphere evolution over the geological timescale (e.g., Towe, 1991; Lawrence and Kamber, 2006). Due to this prominent role, it is essential to avoid artefacts in Ce anomaly calculations that might arise from the La overabundance.

The approach described by Bau and Dulski (1996) and adopted in this paper discriminates positive La and true negative Ce-anomalies: [Ce/Ce* = Ce (SN)/(0.5 Pr (SN) + 0.5 La (SN))] and [Pr/Pr* = (Pr (SN)/(0.5 Ce (SN) + 0.5 Nd (SN))].

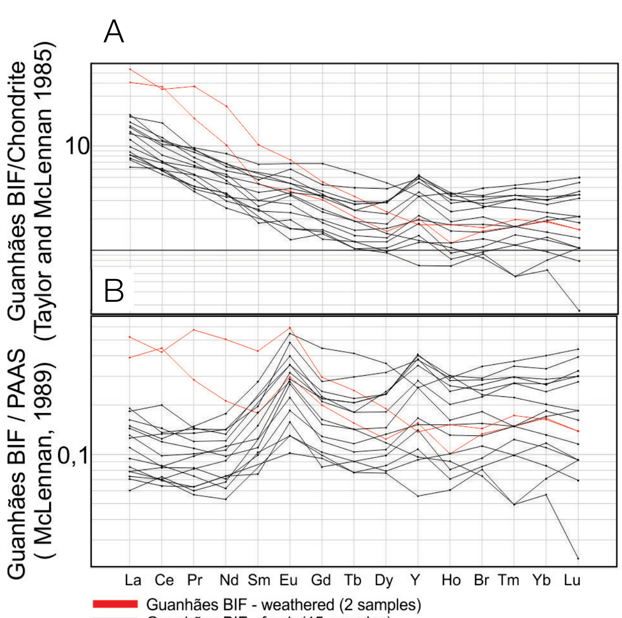

Figure 8. (A) Chondrite-normalized REE spidergram for the Guanhães BIFs. (B) PAAS-normalized REE+Y spidergram for the Guanhães Banded Iron Formations.

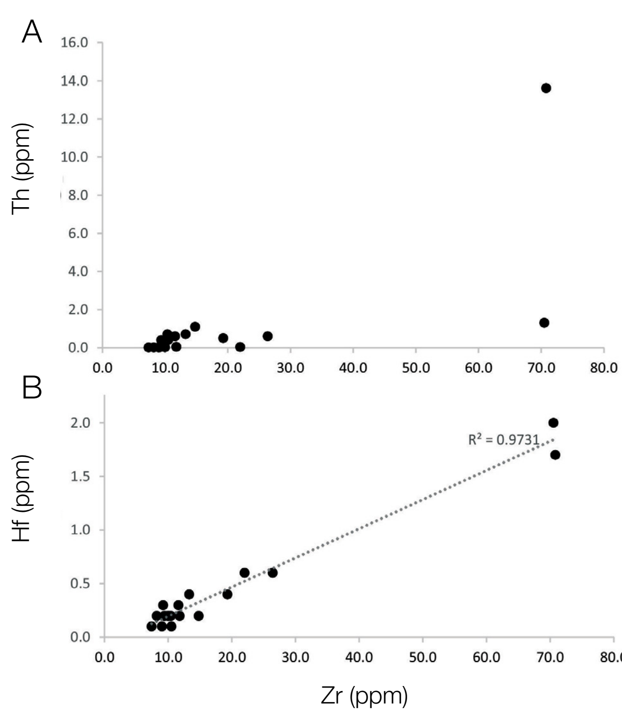

Figure 9. Binary plots of Th and Zr (A) and Hf and Zr (B). Line shows tendency and R2 values are shown.

Five samples with low Y/Ho (squares; Figure 10B) do not present real Ce anomaly, but they show positive Pr anomaly (Pr/Pr* (SN) > 1) plotting outside the usual field reported for BIFs (Planavsky et al., 2010). The carbonate-free samples with higher Y/Ho (circles) display a light positive Ce anomaly, whereas ones containing carbonate show an absence of Ce, La or Pr anomalies (triangles; Figure 11).

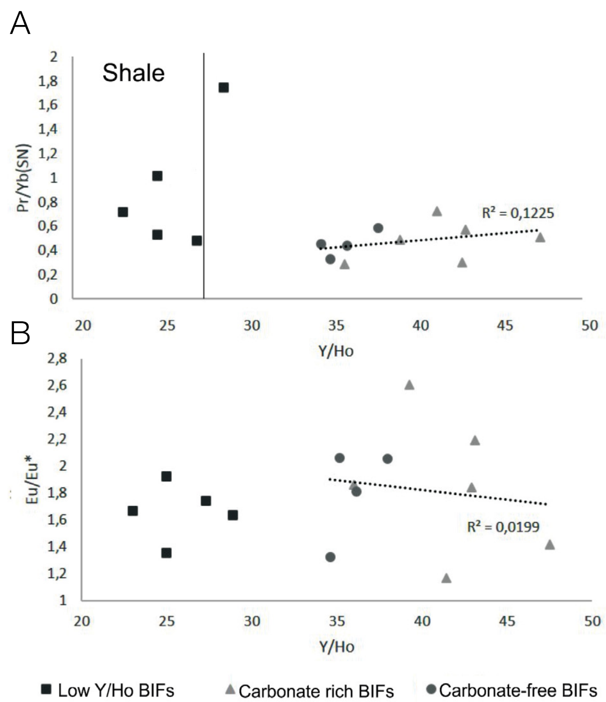

Figure 10. Binary plot of (A) LREE/HREE *versus* Y/Ho. (B) Eu-anomaly *versus* Y/Ho. Lines show tendencies with respective R2 values.

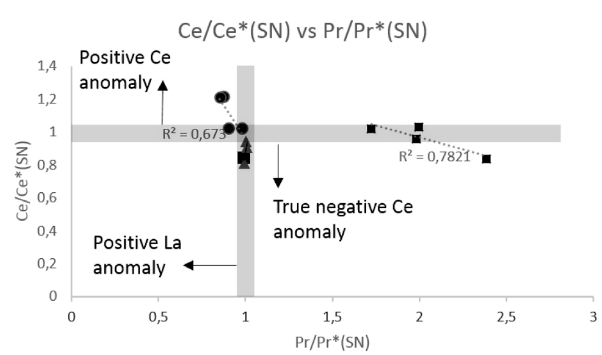

Figure 11. Plot of Ce (SN) and Pr (SN) anomalies. True negative Ce anomalies plots in the field defined by Ce/Ce*(SN) = (CeSN/ (0.5(PrSN + LaSN) > 1 and Pr/Pr*(SN) = (PrSN/ (0.5CeSN + 0.5NdSN)) <1. The approach (Bau and Dulski, 1996) discriminates between positive La and true negative Ce anomalies. Samples that plot in the grey area present neither Ce nor La anomalies (Planavsky et al., 2010).

DISCUSSION

Clastic contamination

Minor amounts of clastic material can result in elevated and correlated abundance of incompatible elements, such as Th, Hf, Zr and Sc. Clastic contamination may also modify the original content of authigenic REE and other trace elements, thus generating anomalous enrichments of redox-sensitive elements like Ce and U.

The Guanhães BIF from the Jambreiro quarry have relatively low TiO_2 (average of 0.3 wt %), Hf (average of 0.5 ppm) and Sc (average of 1.0 ppm for 9 and 8 samples under the detection limit) content, but somewhat elevated concentration of Al_2O_3 (0.35 – 2.01wt %) and Th (average of 12.9 ppm for 15 and 2 samples over 70 ppm). Other pieces of evidence for detrital contamination are provided through the co-variation of the incompatible elements Hf *versus* Zr, as depicted in Figure 9.

Between the Guanhães BIF samples, 5 show strong signatures of terrigenous input, as indicated by the low values of Y/Ho (under 30) plotting in the shale field of the Pr/Y(SN) *versus* Y/Ho plot (Figure 10A). Crustal material has a constant Y/Ho value of ca. 26, whereas seawater-like ratios are > 44 and thus any contamination would depress the seawater signature and lead to negative co-variations (Pecoits, 2010). These samples are contaminated by clastic materials and do not present real Ce anomalies (Figure 11), however they have high Pr/Pr*(SN) values. They are also clearly HREE depleted (Figure 12) and display low Pr/Yb (SN) (Figure 10A).

The chemical indication of clastic contamination, the lack of negative Ce-anomalies and the close association of BIF layers with quartzitic successions (including the occasional occurrence of interbedded quartzite in BIFs) are strong pieces of evidence that these sediments precipitated in a shallow marine environment, with the notable influence of continental input. Another possible explanation for the source of clastic contaminants is the occurrence of sediments from turbiditic sequences; however, there is no sedimentological evidence (e.g., preservation of sedimentary structures) that would indicate the occurrence of metaturbidites in the SSGu.

Nonclastic contamination

Samples without evidence of clastic input can be further subdivided into two groups: (1) hornblende and carbonate-rich BIFs, and (2) BIFs with no carbonate that show distinct REY patterns (Figure 12).

The BIFs with no carbonate display a true positive Ce-anomaly (Figure 11) and Y/Ho close to the chondritic value of 35 (from 35 to 38). They also show higher HREE enrichment, given by the Pr/Yb (SN) ratio (Figure 10A), the slope of the REY-diagram (Figure 12), and the overall higher ΣREE content. These samples do not present the typical seawater La anomaly on the REY-diagram. This suggests some sort of contamination that alters the geochemistry of these postdepositional rocks, creating a pattern that is not similar to the clastic contamination.

Because there is evidence of Cambrian magmatic-driven hydrothermal activity in the region [e.g. zircon U/Pb age data from quartzites, quartz and carbonate veins associated with granites and pegmatites (Barrote, 2016) and metamict zircons associated with hydrothermal xenotime (Rolim, 2016)], a possible contaminant could be younger hydrothermal fluids. The hydrothermal nature of the contaminating fluid could generate such higher positive Eu-anomalies found on those samples (Figures 10B and 12).

New generations of REE-bearing minerals (i.e. crystallized from younger hydrothermal fluids) would alter the REY distribution on those samples, and therefore they would create, for example, a "true" positive Ce-anomaly that does not reflect the redox conditions of BIFs deposition, which is similarly to what was reported by Silveira-Braga et al. (2015) for some of Morro-Escuro BIFs samples containing allanite.

Uncontaminated BIFs

Carbonate-bearing BIFs have the most seawater-like REY-distribution (Figure 12) and Y/Ho values close to 45. These samples lack true Ce anomalies and display REY patterns very similar to the Morro-Escuro BIFs (Figure 13). This could indicate that the presence of carbonates points to uncontaminated BIF. Even though clastic components are probably present in all samples, as indicated by the correlation plot between the incompatible elements Hf *versus* Zr (Figure 9), they are negligible in the hornblende and carbonate-rich BIF samples. The Guanhães BIF has REY-distributions very similar to other Precambrian BIF reported around the world and typical of Archean to Early Proterozoic or Late Proterozoic from oxic to suboxic environments (Planavsky et al., 2010).

The uncontaminated Guanhães BIF displays a REY-distribution pattern (Figure 13) comparable to that of Morro Escuro and Serra da Serpentina BIFs (Figure 1), and shows a similar lack of Ce anomaly, positive Y anomaly, and HREE depletion over LREE and very similar positive Eu anomaly, which indicates that those BIFs could have been formed in similar environments.

Geochronology

SHRIMP data of detrital zircon grains from BIF-related quartzitic units of the SSGu succession suggest a maximum depositional age of ~2.18 Ga derived from the major population in TIGRE1. Even though additional data are necessary for a robust characterization of the ages and populations of source rock and subsequent provenance studies, it is clear that the studied metasedimentary succession is much younger than the Guanhães Complex (2867 ± 10 Ma, Silva et al., 2002) in disagreement with the interpretations of Grossi-Sad (1997).

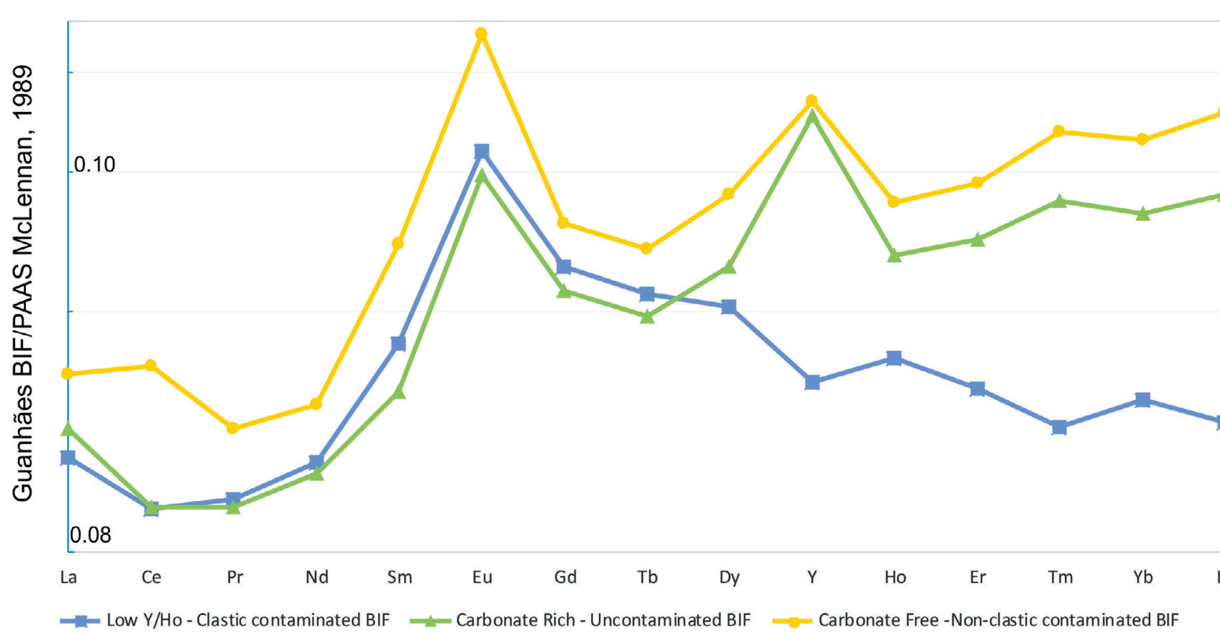

Figure 12. REY spidergram discriminated for each group of sample (average values) from the Guanhães Banded Iron Formation.

The ages of source rocks from the detrital zircons on the lower quartzitic unit are similar to those found by Rolim et al. (2016) for the Meloso Formation, basal to the Serra do Sapo BIF, which presents a large population of Archean zircons with few younger late Paleoproterozoic grains. The upper quartzitic unit shows the prevalence of Archean and Late Orosirian-Rhyacian detrital zircon grains, similarly to the Itapanhoacanga Formation (Rolim et al., 2016). The Guanhães BIF could correlate to the Serra do Sapo Formation, described by Rolim et al. (2016).

There is a correlation between the SSGu's supracrustal units and the stratigraphy proposed by Rolim et al. (2016) for the nearby Serra da Serpentina ridge. The correlation between Serra da Serpentina and Serra de São José groups and the stratigraphy of the central portion of the Southern Espinhaço ridge, as proposed by Rolim el al. (2016), might also be applicable to the SSGu in the Guanhães area, as shown in Figure 14.

The possible source areas for the Archean detrital zircons for the SSGu includes the Guanhães Complex with ages between 2867 and 2711 Ma (Noce et al., 2007), and Rio das Velhas greenstone belt located in the Quadrilátero Ferrífero (Figure 1), in Southern São Francisco Craton (Machado et al., 1996; Hartmann et al., 2006). The Rhyacian peaks are possibly related to the Rhyacian Orogeny (Brito Neves et al., 2014) and potential sources of zircon are rocks from the magmatic-tectonic events of the Minas accretionary event (Teixeira et al., 2015).

CONCLUSIONS

Although the Guanhães BIFs are presented as discontinuous inlets in gneissic terranes, the pieces of evidence of contamination by crustal clastic material and the stratigraphic association with siliciclastic sedimentary rocks indicate that they were deposited in a shallow marine environment.

The dating of detrital zircon of the quartzites is complicated by a strong Cambrian overprint, but it indicates a strong Archean source and a maximum depositional age of

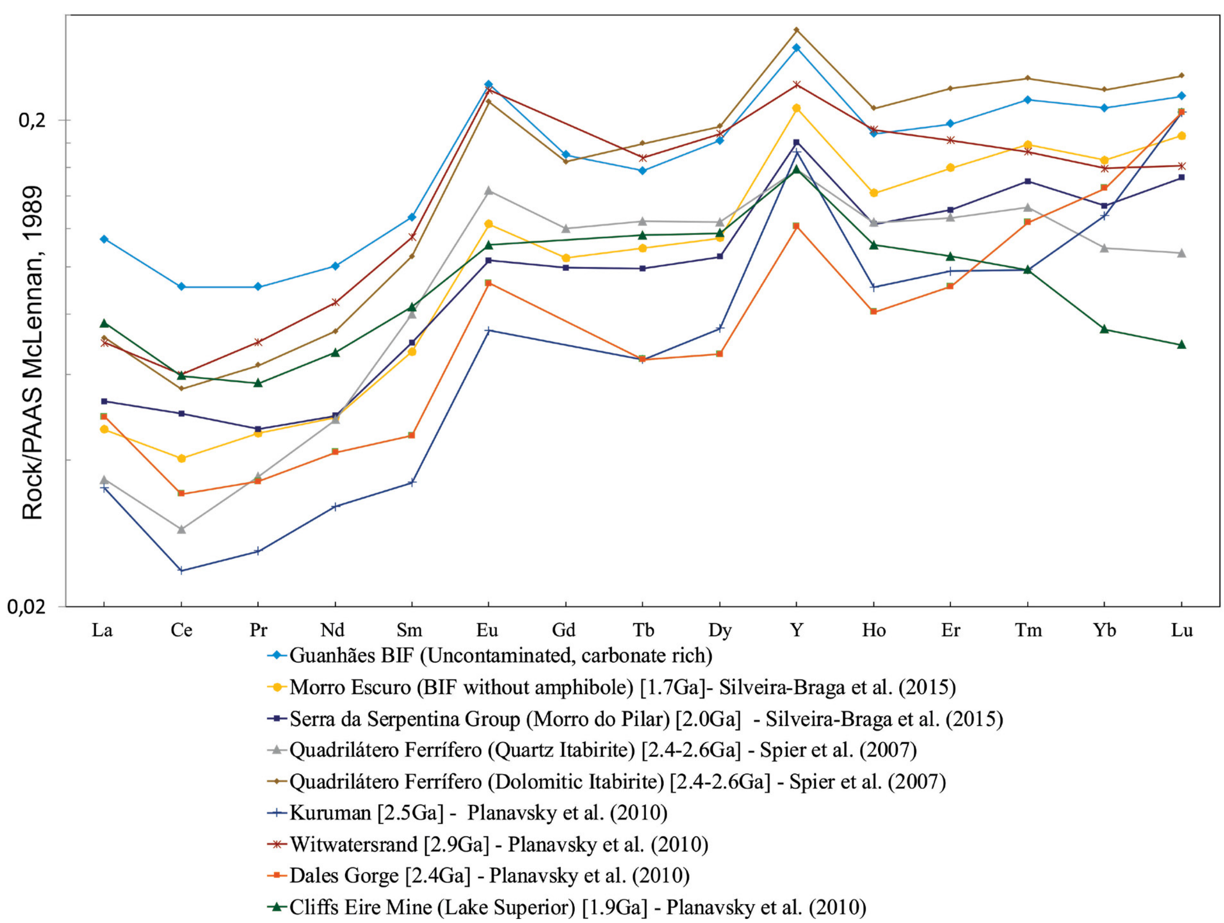

Figure 13. Comparative REY(SN) spidergram for the Guanhães BIF and other worldwide Proterozoic Iron Formations.

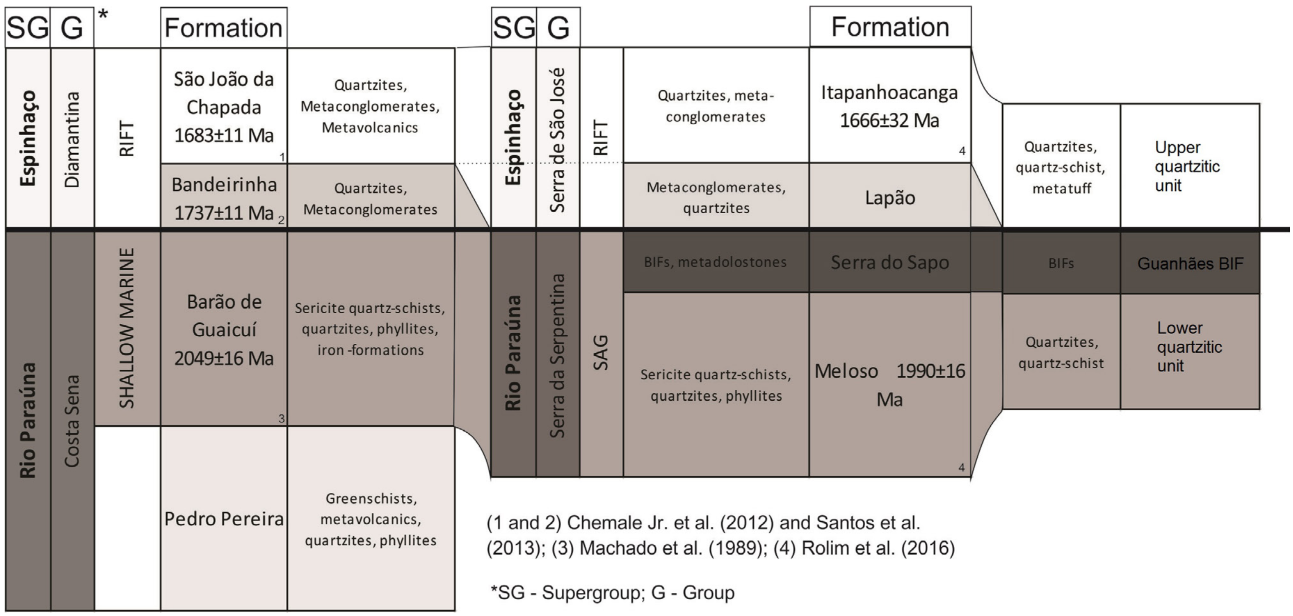

Figure 14. Stratigraphic chart of the Espinhaço Supergroup in the central portion of Southern Espinhaço (modified after Martins-Neto, 2000; Chemale Jr. et al., 2012) correlated to the stratigraphic chart of the Serra da Serpentina and Serra de São José Groups in the Serpentina Range (after Rolim et al., 2016) and to the lithostratigraphic stacking of the SSGuu.

the Guanhães BIF of ~2.18 Ga. Further data are necessary for a robust characterization of the ages and populations of source rock and subsequent provenance studies.

Seawater-like REY signatures are present in BIFs with inter-layered carbonates that broadly preserve the paleoenvironment chemical conditions. Chemically preserved BIF samples have REY distribution (Figure 13) similar to the Morro-Escuro and Serra da Serpentina BIFs from Morro do Pilar (Silveira-Braga et al., 2015; Rolim et al., 2016).

The close association of the Guanhães BIFs with siliciclastic metasediments that display similar distributions of detritic zircon to the quartzitic units of the Meloso and Itapanhoacanga Formation (Rolim et al., 2016) also points to a correlation between SSGu and the Units described at Serra da Serpentina and Serra de São José ridges.

ACKNOWLEGMENTS

The authors are thankful to Centaurus Metals, mainly to R. Fitzhardinge and G. Montresor, and to all the geologists and employees involved in the Jambreiro Project for providing technical support and access to information. They are also grateful for financial resources given by the CNPq (Pr. 473269/2013-9, Pr. 311006/2013-2) and the FAPEMIG, and for the support of CPMTC and all its employees. The authors acknowledge the analytical facilities at Curtin University and the University of Western Australia.

REFERENCES

ACME. (2014). Schedule of Services and Fees (CDN), *Acme Labs*, 41.

Alkmim, F. F., Marshak, S., Pedrosa-Soares, A. C., Peres, G. G., Cruz, S. C., Whittington, A. (2006). Kinematic evolution of the Araçuaí-West Congo orogen in Brazil and Africa: Nutcracker tectonics during the Neoproterozoic assembly of Gondwana. *Precambrian Research*, 149(1-2), 43-64.

Almeida, F. F. M., Hasui, Y., Brito Neves, B. B., Fuck, R. A. (1981). Brazilian structural provinces: an introduction. *Earth Science Review*, 17, 1-29.

Barrote, V. R. (2016). *A sequência portadora de formações ferríferas de Guanhães, Minas Gerais, Brasil.* Dissertação (Mestrado). Belo Horizonte: Instituto de Geociências, Universidade Federal de Minas Gerais.

Bau, M., Dulski, P. (1996). Distribution of yttrium and rare-earth elements in the Penge and Kuruman Iron-Formations, Transvaal Supergroup, South Africa. *Precambrian Research*, 79, 37-55.

Brito Neves, B. B., Fuck, R. A., Pimentel, M. M. (2014). The Brasiliano collage in South America: a review. *Brazilian Journal of Geology*, 44(3), 493-518.

Chemale, Jr., F., Dussin, I. A., Alkmim, F. F., Martins, M. S., Queiroga, G., Armstrong, R., Santos, M. N. (2012). Unravelling a Proterozoic basin history through detrital zircon geochronology: the case of the Espinhaço Supergroup, Minas Gerais. *Gondwana Research*, 22, 200-206.

Dussin, T. M., Duarte, P., Dussin, I. A. (2000). Registro da tectônica Brasiliana na região de Guanhães (SE, Brasil): deformação e metamorfismo das rochas de idade pós-Transamazônicas. *Geonomos*, 8(2), 55-59.

Fernandes, M. L. S. (2001). *O Granito Borrachudos entre Guanhães e Dores de Guanhães (Plutonito Morro do Urubu): Gênese e Evolução.* Tese (Doutorado). Rio de Janeiro: Departamento de Geologia, Universidade Federal do Rio do Janeiro.

Fernandes, M. L. S., Fuzikawa, K., Correia Neves, J. M., Bilal, E., Leonardos, C. M. W. (2000). Fluids related to endoskarn formation process in the Guanhães área, Minas Gerais State, Brazil. *Revista Brasileira de Geociências*, 30(2), 326-330.

Grossi-Sad, J. H. G. (1997). Geologia da Folha Guanhães. In: J. H. G. Grossi-Sad, L. M. Lobato, A. C. P. Soares, B. S. Soares-Filho (Eds.), *Projeto Espinhaço em CD-ROM* (textos, mapas e anexos) (2317-2435). Belo Horizonte: COMIG.

Grossi-Sad, J. H. G., Chiodi Filho, C., Santos, J. F., Magalhães, J. M. M., Carelos, P. M. (1990a). Duas Suítes Graníticas da Borda Sudeste do Cráton Sanfranciscano, em Minas Gerais: Petroquímica e Potencial Metalogenético. In: *XXXVI Congresso Brasileiro de Geologia* (4, 1836-1848). Natal: SBG.

Grossi-Sad, J. H. G., Chiodi Filho, C., Santos, J. F., Magalhães, J. M. M., Carelos, P. M. (1990b). Geoquímica e origem da formação ferrífera do Grupo Guanhães, Distrito de Guanhães, MG, Brasil. In: *XXXVI Congresso Brasileiro de Geologia* (3, 1241-1253). Natal: SBG.

Grossi-Sad, J. H. G., Magalhães, J. M. M., Carelos, P. M. (1989). Geologia do Distrito de Guanhães, Minas Gerais. In: J. H. G. Grossi-Sad, M. A. A. Mourão, M. L. V. Guimarães, L. G. Knauer (1997). *Geologia da Folha Conceição do Mato Dentro.* Relatório Interno. Belo Horizonte: DOCEGEO-GEOSOL.

Hartmann, L. A., Endo, I., Suita, M. T., Santos, J. O. S., Frantz, J. C., Carneiro, M. A., Barley, M. E. (2006). Provenance and age delimitation of Quadrilátero Ferrífero sandstones based on zircon U–Pb isotopes. *Journal of South American Earth Sciences*, 20(4), 273-285.

Knauer, L. G., Grossi-Sad, J. H. G. (1997). Geologia da Folha Serro. In: J. H. G. Grossi-Sad, L. M. Lobato, A. C. P. Soares, B. S. Soares Filho (Eds.), *Projeto Espinhaço, em CD-ROM* (text and maps) (2057-2316). Belo Horizonte: COMIG - Companhia Mineradora de Minas Gerais.

Lawrence, M. G., Kamber, B. S. (2006). The behaviour of the rare earth elements during estuarine mixing-revisited. *Marine Chemistry*, 100(1-2), 147-161.

Ludwig, K. R. (2001). SQUID 1.02: a User's Manual. *Berkeley Geochronology Centre*, 2, 19. Special Publication.

Ludwig, K. R. (2003). ISOPLOT 3.00 e a Geochronological Toolkit for Excel. *Berkeley Geochronology Center*, 4, 67. Special Publication.

Machado, N., Schrank, A., Abreu, F. R., Knauer, L. G., Almeida-Abreu, P. A. (1989). Resultados preliminares da geocronologia U/Pb na Serra do Espinhaço Meridional. *Boletim da Sociedade Brasileira de Geologia, Núcleo Minas Gerais*, 10, 171-174.

Machado, N., Schrank, A., Noce, C. M., Gauthier, G. (1996). Ages of detrital zircon from Archean– Paleoproterozoic sequences: implications for greenstone belt setting and evolution of a Transamazonian foreland basin in Quadrilátero Ferrífero, southeast Brazil. *Earth and Planetary Science Letters*, 141, 259-276.

Martins-Neto, M. A. (2000) Tectonics and sedimentation in a Paleomesoproterozoic rift-sag basin (Espinhaço basin, southeastern Brazil). *Precambrian Research*, 103, 147-173.

McLennan, S. M. (1989). Rare earth elements in sedimentary rocks: influence of provenance and sedimentary processes. In: B. R. Lipin, G. A. McKay (Eds.), Geochemistry and Mineralogy of Rare Earth Elements, *Reviews in Mineralogy*, 21, 169-200.

Noce, C. M., Soares, A. C. P., Silva, L. C., Alkmim, F. F. (2007). O Embasamento Arqueano e Paleoproterozoico do Orógeno Araçuaí. *Geonomos*, 15(1), 17-23.

Pecoits, E. (2010). *Ediacaran Iron Formations and Carbonates of Uruguay: Palaeoceanographic, Palaeoclimatic and Palaeobiologic Implications*. PhD thesis. Edmonton: University of Alberta.

Pedrosa-Soares, A. C., Noce, C. M. (1998). Where is the suture zone of the Neoproterozoic Araçuaí-West-Congo orogen? In: *XIV Conference on Basement Tectonics* (35-37). Ouro Preto: UFOP.

Pedrosa-Soares, A. C., Noce, C. M., Alkmim, F. F., Silva, L. C., Babinski, M., Cordani, U., Castañeda, C. (2007). Orógeno Araçuaí: síntese do conhecimento 30 anos após Almeida 1977. *Geonomos*, 15, 1-16.

Pedrosa-Soares, A. C., Noce, C. M., Wiedemann, C. M., Pinto, C. P. (2001). The Araçuaí–West Congo orogen in Brazil: An overview of a confined orogen formed during Gondwanland assembly. *Precambrian Research*, 110, 307-323.

Pedrosa-Soares, A. C., Wiedemann-Leonardos, C. M. (2000). Evolution of the Araçuaí Belt and its connection to the Ribeira Belt, Eastern Brazil. In: U. Cordani, E. Milani, A. Thomaz-Filho, D. A. Campos (Eds.), *Tectonic Evolution of South America* (265-285). São Paulo: SBG.

Pedrosa Soares, A. C. P., Dardenne, M. A., Hasui, Y., Castro, F. D. C., Carvalho, M. V. A. (1994). *Nota Explicativa dos Mapas Geológico, Metalogenético e de Ocorrências Minerais do Estado de Minas Gerais*. Escala 1:1.000.000. Minas Gerais: Companhia Mineradora de Minas Gerais – COMIG.

Planavsky, N., Bekker, A., Rouxel, O. J., Kamber, B., Hofmann, A., Knudsen, A., Lyons, T. W. (2010). Rare earth element and yttrium compositions of Archean and Paleoproterozoic Fe formations revisited: new perspectives on the significance and mechanisms of deposition. *Geochimica et Cosmochimica Acta*, 74(22), 6387-6405.

Rolim, V. K. (2016). *As formações ferríferas da região de Conceição Do Mato Dentro - MG: Posicionamento estratigráfico, evolução tectônica, geocronologia, características geoquímicas e gênese dos minérios.* Tese (Doutorado). Belo Horizonte: Instituto de Geociências, Universidade Federal de Minas Gerais.

Rolim, V. K., Rosière, C. A., Santos, J. O. S., McNaughton, N. J. (2016). The Orosirian-Statherian banded iron formation-bearing sequences of the southern border of the Espinhaço range, southeast Brazil. *Journal of South American Earth Sciences*, 65, 43-66.

Santos, M. N., Chemale Jr., F., Dussin, I. A., Martins, M., Assis, T. A. R., Jelinek, A. R., Guadagnin, F., Armstrong, R. (2013). Sedimentological and paleoenvironmental constraints of the Statherian and Stenian Espinhaço rift system, Brazil. *Sedimentary Geology*, 290, 47-59.

Silva, L. C., Armstrong, R., Noce, C. M., Carneiro, M. A., Pimentel, M. M., Pedrosa-Soares, A. C., Leite, C. A., Vieira, V. S., Silva, M. A., Paes, V. J. C., Cardoso Filho, J. M. (2002a). Reavaliação da evolução geológica em terrenos pré-cambrianos brasileiros com base em novos dados U-Pb SHRIMP, parte II: Orógeno Araçuaí, Cinturão Mineiro e Cráton São Francisco Meridional. *Revista Brasileira de Geociências*, 32(4), 513-528.

Silveira-Braga, F. C., Rosière, C. A., Queiroga, G. N., Rolim, V. K., Santos, J. O. S., McNaughton, N. J. (2015). The Statherian itabirite-bearing sequence from the Morro Escuro Ridge, Santa Maria de Itabira, Minas Gerais, Brazil. *Journal of South American Earth Sciences*, 58, 33-53.

Spier, C. A., Oliveira, S. M. B., Sial, A. N., Rios, F. J. (2007). Geochemistry and genesis of the banded iron formations of the Cauê Formation, Quadrilátero Ferrífero, Minas Gerais, Brazil. *Precambrian Research*, 152, 170-206.

Taylor, S. R., McLennan, S. M. (1985). *The Continental Crust: Its Composition and Evolution*. London: Blackwell.

Teixeira, W., Ávila, C. A., Dussin, I. A., Corrêa Neto, A. V., Bongiolo, E. M., Santos, J. O., Barbosa, N. S. (2015). A juvenile accretion episode (2.35–2.32 Ga) in the Mineiro belt and its role to the Minas accretionary orogeny: Zircon U–Pb–Hf and geochemical evidences. *Precambrian Research*, 256, 148-169.

Towe, K. M. (1991). Aerobic carbon cycling and cerium oxidation: significance for Archean oxygen levels and banded iron-formation deposition. *Global and Planetary Change*, 5(1-2), 113-123.

Vermeesch, P. (2004). How many grains are needed for a provenance study? *Earth and Planetary Science Letters*, 224(3-4), 441-451.

Appendix A. Table of U-Pb data of detrital and hydrothermalized zircon of quartzites of Guanhães Group.

Spot	U	Th	$^{232}Th/^{238}U$	^{206}Pb	comm. ^{206}Pb	Isotopic Ratios $^{207}Pb/^{206}Pb$	error	$^{207}Pb/^{235}U$	error	$^{206}Pb/^{238}U$	err	error corr.	$^{208}Pb/^{232}Th$	error	$^{206}Pb/^{238}U$	error	Ages $^{207}Pb/^{206}Pb$	error	σ $^{207}Pb/^{206}Pb$	error	Disc.
Spot	ppm	ppm		ppm	%		1σ %		1σ %		1σ %			1σ %	Age	1σ	Age[1]	1σ	Age[2]	1σ	%
Cinza1																					
b.1-1	27	2	0.06	2.5	0	0.11123	4.16	1.6618	5.01	0.1084	2.79	0.556	0.1129	9.13	663	18	1820	76	2971	11	63.6
b.1-2	242	118	0.5	93.5	0.01	0.2119	0.58	13.1436	1.14	0.4499	0.99	0.863	0.1013	1.67	2395	20	2920	9	2971	11	18
b.1-3	149	68	0.47	62.8	0.07	0.20226	0.68	13.6466	1.3	0.4894	1.11	0.852	0.1322	1.77	2568	23	2844	11	2843	11	9.7
b.1-4	63	61	1	31.7	-0.02	0.27215	1.12	21.9149	2.05	0.584	1.71	0.836	0.1648	2.21	2965	41	3318	18	3318	18	10.6
b.2-1	158	88	0.57	68.5	0.09	0.21852	0.48	15.2367	1.61	0.5057	1.54	0.955	0.1539	1.8	2638	33	2970	8	2970	11	11.2
b.2-2	244	111	0.47	89.8	0.11	0.20105	0.49	11.8619	1.64	0.4279	1.57	0.955	0.124	2.03	2296	30	2835	8	2843	11	19
b.2-3	109	71	0.67	47.7	0.11	0.21002	0.68	14.7381	1.8	0.5089	1.67	0.925	0.1382	2.12	2652	36	2906	11	2930	9	8.7
b.2-4	617	24	0.04	42.8	0.18	0.05724	1.48	0.6361	2.11	0.0806	1.5	0.71	0.0231	13.63	499.6	7.2	501	33	501	33	0.3
b.2-5	107	50	0.48	52.5	0.08	0.21856	0.72	17.1123	1.44	0.5678	1.24	0.865	0.1488	2.05	2899	29	2970	12	2971	11	2.4
b.2-6	133	58	0.46	59	0	0.20639	0.85	14.7193	1.53	0.5173	1.27	0.83	0.1432	2.08	2688	28	2877	14	2884	18	6.6
b.2-8	195	101	0.53	83.6	0.09	0.20229	0.65	13.8959	1.26	0.4982	1.08	0.857	0.135	1.71	2606	23	2845	11	2843	11	8.4
b.2-9	165	99	0.62	71.3	0.02	0.20051	0.71	13.9042	1.3	0.5029	1.1	0.84	0.1381	1.52	2626	24	2830	12	2843	11	7.2
b.5-1	136	37	0.28	46.8	0.2	0.20349	0.78	11.196	1.9	0.399	1.73	0.912	0.1023	3.72	2165	32	2854	13	2884	18	24.2
b.6-1	82	61	0.78	38.2	0.14	0.2013	0.84	15.1011	1.96	0.5441	1.77	0.904	0.1459	2.33	2801	40	2837	14	2843	11	1.3
b.6-2	93	43	0.47	42.3	0.13	0.20076	0.81	14.5778	1.92	0.5266	1.74	0.907	0.1381	3.04	2727	39	2832	13	2843	11	3.7
b.6-3	131	138	1.08	65.9	0.01	0.22579	0.55	18.178	1.82	0.5839	1.73	0.953	0.1552	2.79	2965	41	3022	9	3022	9	1.9
b.6-4	81	37	0.46	32.2	-0.06	0.19439	1.09	12.3551	2.05	0.461	1.73	0.846	0.1247	3.13	2444	35	2780	18	2811	12	12.1
b.7-1	173	46	0.27	74.1	0.16	0.21497	0.55	14.7971	1.68	0.4992	1.59	0.945	0.128	2.63	2610	34	2943	9	2971	11	11.3
b.7-2	124	104	0.87	56.2	0.11	0.20043	0.88	14.5328	1.95	0.5259	1.74	0.893	0.1425	2.01	2724	39	2830	14	2843	11	3.7
b.8-1	79	35	0.46	24.1	0.17	0.19601	0.94	9.5489	2.01	0.3533	1.78	0.883	0.1207	3.06	1950	30	2793	15	2843	11	30.2
b.8-2	101	64	0.66	50.1	0	0.2133	0.77	17.0356	1.87	0.5792	1.71	0.912	0.1528	1.98	2946	40	2931	12	2930	9	-0.5
b.8-3	174	104	0.62	70.9	0.12	0.18569	0.6	12.0972	1.7	0.4725	1.59	0.936	0.1288	1.95	2495	33	2704	10	2734	15	7.8
b.8-4	33	12	0.37	15.9	0.19	0.21692	1.36	16.5341	2.6	0.5528	2.21	0.853	0.1525	5.56	2837	51	2958	22	2971	11	4.1
b.9-1	133	55	0.43	59.7	0.04	0.18706	2.53	13.4347	3.12	0.5209	1.83	0.586	0.1325	3.37	2703	40	2716	42	2734	15	0.5
b.9-2	175	115	0.68	93.8	0.06	0.26754	0.43	22.966	1.64	0.6226	1.58	0.965	0.1668	1.77	3120	39	3292	7	3292	7	5.2

Continue...

Appendix A. Continuation.

						Isotopic Ratios									Ages				σ		
Spot	U	Th	$^{232}Th/^{238}U$	^{206}Pb	comm. ^{206}Pb	$^{207}Pb/^{206}Pb$	error	$^{207}Pb/^{235}U$	error	$^{206}Pb/^{238}U$	err	error corr.	$^{208}Pb/^{232}Th$	error	$^{206}Pb/^{238}U$	error	$^{207}Pb/^{206}Pb$	error	$^{207}Pb/^{206}Pb$	error	Disc.
Spot	ppm	ppm		ppm	%		1σ %		1σ %		1σ %			1σ %	Age	1σ	Age[1]	1σ	Age[2]	1σ	%
b.10-1	120	126	1.09	35.9	0.22	0.17352	0.91	8.3009	1.9	0.347	1.67	0.877	0.1099	2.21	1920	28	2592	15	2734	15	25.9
b.10-2	68	51	0.78	28.5	0.24	0.21171	1	14.2413	2.08	0.4879	1.82	0.876	0.1354	2.51	2561	38	2919	16	2971	11	12.2
b.10-3	296	196	0.68	121.7	0.06	0.21155	0.47	13.9397	1.59	0.4779	1.52	0.956	0.128	1.7	2518	32	2917	8	2971	11	13.7
b.10-4	147	93	0.65	56	0.06	0.19226	0.64	11.7725	1.74	0.4441	1.62	0.931	0.1361	1.94	2369	32	2762	10	2811	12	14.2
b.12-1	24	12	0.51	11.2	0.26	0.20293	1.45	14.9683	2.8	0.535	2.39	0.856	0.1383	4.13	2762	54	2850	24	2843	11	3.1
b.12-2	141	47	0.34	53	0.08	0.17674	0.77	10.6768	1.81	0.4381	1.64	0.905	0.1247	2.93	2342	32	2623	13	2658	15	10.7
b.12-3	454	15	0.03	32.3	0	0.05761	1.28	0.6588	2	0.0829	1.53	0.767	0.0301	4.76	513.6	7.6	515	28	515	28	0.2
Tigre1																					
f.1-1	145	83	0.59	54	0.13	0.16034	0.84	9.5582	1.82	0.4323	1.62	0.888	0.1174	2.15	2316	31	2459	14	2457	11	5.8
f.1-2	58	37	0.66	19.4	0	0.1363	1.33	7.3819	2.38	0.3928	1.98	0.831	0.1098	2.68	2136	36	2181	23	2192	12	2.1
f.1-3	154	63	0.42	64.3	0.05	0.18325	0.7	12.2427	1.77	0.4846	1.62	0.917	0.1303	2.29	2547	34	2682	12	2702	7	5
f.1-4	142	103	0.75	48.1	0.07	0.13657	0.89	7.4166	1.87	0.3939	1.65	0.88	0.1071	2.06	2141	30	2184	15	2192	12	2
f.1-5	92	44	0.49	36.3	0	0.17534	0.87	11.0995	2.05	0.4591	1.86	0.906	0.1207	2.35	2436	38	2609	14	2632	14	6.7
f.1-6	359	3	0.01	25	0	0.05716	2.22	0.6384	2.52	0.081	1.18	0.469	0.023	15.13	502.1	5.7	498	49	502	5	-0.9
f.2-1	225	146	0.67	71.2	0.06	0.13609	0.65	6.9187	1.67	0.3687	1.53	0.92	0.1004	1.78	2023	27	2178	11	2192	12	7.1
f.2-2	124	60	0.5	50.2	0.01	0.18389	0.61	11.9643	1.17	0.4719	1	0.855	0.1288	1.52	2492	21	2688	10	2702	7	7.3
f.2-3	119	60	0.52	62.2	0.04	0.249	0.92	20.8142	1.46	0.6063	1.13	0.776	0.1545	2.07	3055	27	3178	15	3189	15	3.9
f.2-4	23	9	0.4	8.1	0.15	0.1362	2.07	7.5727	2.86	0.4033	1.97	0.688	0.1234	5.73	2184	36	2179	36	2192	12	-0.2
f.3-1	212	94	0.46	82.1	-0.12	0.18243	0.68	11.3607	1.9	0.4517	1.78	0.935	0.1279	2.31	2403	36	2675	11	2702	7	10.2
f.3-2	221	121	0.56	67.7	0.03	0.13523	0.77	6.6274	1.71	0.3554	1.53	0.892	0.1007	2.01	1961	26	2167	13	2192	12	9.5
f.3-3	152	59	0.4	64.9	0.26	0.17065	1.39	11.6373	2.2	0.4946	1.7	0.774	0.1656	2.63	2591	36	2564	23	2561	23	-1
f.3-4	152	59	0.4	43.4	0	0.17303	1.29	7.9142	1.68	0.3317	1.07	0.64	0.1161	1.52	1847	17	2587	21	2702	7	28.6
f.3-5b	64	57	0.93	25.7	0.02	0.18791	1.28	12.1749	1.79	0.4699	1.25	0.7	0.1298	1.69	2483	26	2724	21	2754	21	8.8
f.3-6	97	80	0.86	28.5	0.19	0.13205	1.04	6.2377	1.6	0.3426	1.22	0.759	0.1092	1.73	1899	20	2125	18	2192	12	10.6
f.3-7	109	67	0.64	37.2	-0.01	0.13684	0.77	7.4617	2.02	0.3955	1.86	0.925	0.1096	2.16	2148	34	2188	13	2192	12	1.8
f.3-8	204	66	0.33	57.2	0.02	0.13566	0.63	6.1049	1.17	0.3264	0.99	0.842	0.0955	1.55	1821	16	2173	11	2248	11	16.2

Continue...

Appendix A. Continuation.

Spot	U	Th	$^{232}Th/^{238}U$	^{206}Pb	comm. ^{206}Pb	$^{207}Pb/^{206}Pb$	error	$^{207}Pb/^{235}U$	error	$^{206}Pb/^{238}U$	err	error corr.	$^{208}Pb/^{232}Th$	error	$^{206}Pb/^{238}U$	error	$^{207}Pb/^{206}Pb$	error	$^{207}Pb/^{206}Pb$	error	Disc.
						Isotopic Ratios									Ages				σ		
Spot	ppm	ppm		ppm	%		1σ %		1σ %		1σ %			1σ %	Age	1σ	Age[1]	1σ	Age[2]	1σ	%
f.4-1	646	7	0.01	46.1	0.04	0.05783	1.07	0.6615	1.28	0.083	0.69	0.543	0.0273	19.03	513.8	3.4	523	24	514	4	1.8
f.4-2	180	63	0.36	40	0.28	0.12369	0.82	4.3882	2.2	0.2572	2.04	0.928	0.0809	2.46	1476	27	2011	15	2192	12	26.6
f.4-3	420	2	0.01	30	0.04	0.05766	1.22	0.6606	1.44	0.0831	0.78	0.539	0.0392	18.45	514.6	3.9	517	27	515	4	0.4
f.4-4	57	16	0.29	22.4	0	0.15978	1.03	10.0082	2.53	0.4543	2.31	0.913	0.1309	3.11	2414	46	2453	17	2457	11	1.6
f.4-5	146	71	0.5	65.9	0.03	0.18506	0.71	13.3653	1.79	0.5238	1.64	0.918	0.1457	2.12	2715	36	2699	12	2702	7	-0.6
f.4-6	468	3	0.01	32.8	0	0.05805	1.98	0.6519	2.23	0.0814	1.03	0.46	0.0281	12.85	504.8	5	532	43	505	5	5.1
f.4-7	136	72	0.55	43	0	0.13561	0.96	6.8807	2	0.368	1.75	0.878	0.1046	2.24	2020	30	2172	17	2192	12	7
f.4-8	118	58	0.51	37.7	0.06	0.15227	0.84	7.8188	1.85	0.3724	1.65	0.89	0.1045	2.26	2041	29	2372	14	2414	16	14
f.4-9	204	213	1.08	93.4	0	0.19866	0.55	14.5807	1.65	0.5323	1.55	0.942	0.1442	1.71	2751	35	2815	9	2822	9	2.3
f.4-10	162	65	0.42	59.8	0	0.17771	0.73	10.4962	1.76	0.4284	1.61	0.911	0.1191	2.08	2298	31	2632	12	2678	13	12.7
f.4-11	157	35	0.23	35.5	0.46	0.12656	1.32	4.5664	1.72	0.2617	1.1	0.64	0.0779	5.67	1499	15	2051	23	2192	12	26.9
f.5-1	114	88	0.8	43.7	0	0.1555	1.05	9.6031	2.01	0.4479	1.72	0.854	0.1255	2.08	2386	34	2407	18	2414	16	0.9
f.5-2	62	24	0.39	23.5	0	0.156	1.12	9.4264	2.2	0.4382	1.9	0.861	0.1302	2.74	2343	37	2413	19	2414	16	2.9
f.6-1	265	131	0.51	75.3	0.06	0.13236	0.61	6.0317	2.09	0.3305	2	0.956	0.0966	2.21	1841	32	2130	11	2192	12	13.6
f.6-2	93	60	0.67	31	0.22	0.13263	1.24	7.1242	1.59	0.3896	1	0.628	0.0805	2.65	2121	18	2133	22	2135	22	0.6
f.7-1	181	136	0.78	61.1	-0.01	0.13343	0.78	7.221	1.15	0.3925	0.85	0.738	0.1131	1.41	2134	15	2144	14	2145	14	0.4
Candonga																					
g.1-1	150	82	0.57	72	0	0.20205	0.7	15.5857	1.81	0.5595	1.67	0.922	0.1504	2.05	2864	39	2843	11	2841	11	-0.8
g.1-2	41	15	0.38	22.7	0.19	0.26903	1.4	24.1186	2.59	0.6502	2.18	0.841	0.1752	5.54	3229	55	3300	22	3292	9	2.2
g.1-3	164	119	0.75	63.1	0	0.18741	0.65	11.5378	1.8	0.4465	1.68	0.933	0.1219	1.91	2380	33	2720	11	2764	11	12.5
g.1-4	143	72	0.52	57.4	0.01	0.18316	0.71	11.8196	1.85	0.468	1.71	0.924	0.1298	2.1	2475	35	2682	12	2702	7	7.7
g.1-5	190	97	0.53	79.9	-0.02	0.21656	0.5	14.6339	1.15	0.4901	1.04	0.901	0.137	2.04	2571	22	2955	8	2980	8	13
g.1-6	76	38	0.52	29.2	-0.02	0.20251	0.77	12.4889	1.42	0.4473	1.19	0.839	0.1311	1.77	2383	24	2847	13	2904	14	16.3
g.1-7	603	52	0.09	75.6	0.01	0.12801	2.82	2.5767	2.95	0.146	0.84	0.286	0.036	3.22	878.4	6.9	2071	50	2838	50	57.6
g.2-1	142	47	0.34	64.8	0.03	0.21583	0.94	15.8395	1.88	0.5323	1.63	0.867	0.1396	2.89	2751	37	2956	15	2980	8	6.7
g.2-2-1	155	81	0.54	59.1	0	0.20093	0.66	12.27	1.24	0.4429	1.05	0.847	0.1266	1.52	2364	21	2834	11	2893	12	16.6

Continue...

Appendix A. Continuation.

Spot	U	Th	$^{232}Th/^{238}U$	^{206}Pb	comm. ^{206}Pb	Isotopic Ratios $^{207}Pb/^{206}Pb$	error	$^{207}Pb/^{235}U$	error	$^{206}Pb/^{238}U$	err	error corr.	$^{208}Pb/^{232}Th$	error	$^{206}Pb/^{238}U$	error	Ages $^{207}Pb/^{206}Pb$	error	σ $^{207}Pb/^{206}Pb$	error	Disc.
Spot	ppm	ppm		ppm	%		1σ %		1σ %		1σ %			1σ %	Age	1σ	Age[1]	1σ	Age[2]	1σ	%
g.2-3	329	289	0.91	109.3	0	0.1644	0.43	8.7617	0.98	0.3865	0.88	0.899	0.1101	1.13	2107	16	2501	7	2565	7	15.8
g.2-4	53	27	0.52	21.4	0.16	0.22447	0.94	14.5152	1.64	0.469	1.35	0.821	0.1215	2.71	2479	28	3013	15	3074	15	17.7
g.2-5	250	176	0.73	59.8	0.05	0.10428	0.73	4.0088	1.15	0.2788	0.89	0.77	0.0833	1.23	1585	12	1702	14	1737	14	6.8
g.2-6	162	96	0.61	87.5	0.04	0.28766	0.5	24.9186	1.09	0.6283	0.97	0.89	0.1642	1.46	3143	24	3405	8	3405	8	7.7
g.2-7	202	98	0.5	82.7	-0.06	0.22148	0.75	14.5763	1.24	0.4773	0.99	0.796	0.1384	1.38	2516	21	2991	12	3045	12	15.9
g.2-8	235	135	0.59	92.9	0.04	0.20632	0.48	13.0825	1.07	0.4599	0.96	0.895	0.132	1.31	2439	20	2877	8	2930	8	15.2
g.3-1	51	23	0.47	26.9	0	0.23463	1.04	19.9836	2.51	0.6177	2.28	0.91	0.1636	3.06	3101	56	3084	17	3084	17	-0.5
g.3-2	118	72	0.63	58.7	0.01	0.21882	0.73	17.4482	1.97	0.5783	1.83	0.928	0.1561	2.21	2942	43	2972	12	2980	8	1
g.3-3	165	10	0.06	59.6	0	0.23664	0.78	13.7046	1.82	0.42	1.64	0.903	0.115	4.11	2261	31	3098	12	3292	9	27
g.3-4	71	33	0.48	37.2	0	0.2215	0.93	18.7319	2.16	0.6134	1.95	0.902	0.1638	2.62	3084	48	2992	15	2980	8	-3.1
g.3-5	519	24	0.05	37	0	0.05706	2.05	0.6521	2.24	0.0829	0.9	0.403	0.0267	4.23	513.3	4.5	496	45	513	5	-4
g.3-6	31	9	0.31	15.4	0	0.2154	1.02	17.2	1.92	0.5791	1.63	0.848	0.153	2.82	2945	38	2947	16	2943	15	0
g.4-1	84	48	0.6	36.1	0	0.21643	0.93	14.9833	2.08	0.5021	1.86	0.895	0.1436	2.41	2623	40	2954	15	2980	8	11.2
g.4-2	50	15	0.32	22.9	0	0.22005	0.99	16.2301	2.38	0.5349	2.17	0.91	0.1466	3.12	2762	49	2981	16	2980	8	7.3
g.4-3	57	12	0.22	26.8	0.18	0.21868	1.04	16.5724	1.79	0.5496	1.47	0.817	0.1431	6.55	2824	34	2971	17	2980	8	5
g.4-4	54	49	0.94	30.6	-0.01	0.26718	0.71	24.3542	1.51	0.6611	1.33	0.882	0.1753	1.71	3271	34	3290	11	3292	9	0.6
g.4-5	57	30	0.54	33.1	-0.1	0.26745	0.76	24.8144	1.49	0.6729	1.28	0.86	0.1734	2.04	3317	33	3291	12	3292	9	-0.8
g.5-1-5	355	15	0.04	24.3	0	0.05689	2.19	0.6259	2.42	0.0798	1.03	0.425	0.0295	5.84	494.9	4.9	487	48	495	5	-1.6
g.5-2	193	109	0.59	87.5	0.03	0.21244	0.51	15.427	1.1	0.5267	0.97	0.886	0.1407	1.32	2727	22	2924	8	2943	15	6.7
g.5-3	183	155	0.88	77.5	0.06	0.24893	0.51	16.9308	1.2	0.4933	1.09	0.906	0.1365	1.36	2585	23	3178	8	3292	9	18.7
g.5-4	408	48	0.12	28.1	0.2	0.05704	1.47	0.6289	1.75	0.08	0.94	0.539	0.0227	3.24	495.9	4.5	493	32	496	5	-0.5
g.6-1	1102	22	0.02	81.2	0.2	0.05761	1.85	0.6799	2.35	0.0856	1.44	0.615	0.0175	57.46	529.5	7.3	515	41	530	7	-2.8
g.6-2	806	18	0.02	57.3	0	0.05962	1.22	0.6796	1.46	0.0827	0.81	0.553	0.0351	3.97	512.1	4	590	26	512	4	13.2
g.6-3	313	109	0.36	135.4	-0.02	0.21184	0.36	14.6973	0.91	0.5032	0.84	0.919	0.1364	1.72	2628	18	2920	6	2943	15	10
g.6-4	45	20	0.47	21.6	0.19	0.19497	1.24	14.9785	2.47	0.5572	2.14	0.866	0.1408	3.63	2855	49.4	2785	20	2777	20	-2.5
Peçanha3																					
c.2-1	166	85	0.53	69	0.07	0.20006	0.54	13.37	1.66	0.4845	1.57	0.946	0.1355	1.87	2547	33	2827	9	2858	10	9.9

Continue...

Appendix A. Continuation.

Spot	U	Th	$^{232}Th/^{238}U$	^{206}Pb	comm. ^{206}Pb	$^{207}Pb/^{206}Pb$	error	$^{207}Pb/^{235}U$	error	$^{206}Pb/^{238}U$	err	error corr.	$^{208}Pb/^{232}Th$	error	$^{206}Pb/^{238}U$	error	$^{207}Pb/^{206}Pb$	error	$^{207}Pb/^{206}Pb$	error	Disc.
			Isotopic Ratios												Ages				σ		
Spot	ppm	ppm		ppm	%		1σ %		1σ %		1σ %			1σ %	Age	1σ	Age[1]	1σ	Age[2]	1σ	%
c.2-2	37	16	0.45	17.4	0.21	0.20976	1.12	15.65	2.33	0.5412	2.04	0.876	0.1474	4.13	2788	46	2904	18	2915	20	4
c.2-3	1621	108	0.07	110.6	0.09	0.05772	1.07	0.63	1.31	0.0793	0.76	0.578	0.0244	6.11	492.1	3.6	519	24	519	24	5.2
c.3-1	141	46	0.34	81.5	0.09	0.30546	0.43	28.24	1.82	0.6706	1.77	0.972	0.18	2.2	3308	46	3498	7	3511	8	5.4
c.3-2	133	52	0.4	55.5	0.09	0.20659	0.6	13.85	1.71	0.4862	1.6	0.936	0.1369	2.2	2554	34	2879	10	2915	11	11.3
c.3-4	96	27	0.3	20.1	0.16	0.18765	1.98	6.32	2.41	0.2443	1.37	0.567	0.081	3.97	1409	17	2722	33	3039	42	48.2
c.3-5	236	153	0.67	72.7	0.1	0.192	0.69	9.49	1.3	0.3586	1.1	0.849	0.1041	1.57	1976	19	2759	11	2882	14	28.4
c.4-1	917	31	0.04	65.2	0	0.05849	1.21	0.667	1.36	0.0827	0.62	0.459	0.0278	4.27	512.2	3.1	548	26	548	26	6.6
c.4-2	142	64	0.47	49.4	0	0.19957	0.73	11.12	1.37	0.4041	1.16	0.845	0.1104	1.77	2188	21	2823	12	2909	14	22.5
c.5-1-2	111	67	0.62	44.5	0	0.20967	1.44	13.47	2.03	0.4659	1.44	0.708	0.1285	2.27	2466	29	2903	23	2953	26	15.1
c.5-2	148	77	0.54	61.3	0.03	0.21363	0.76	14.2006	1.32	0.4821	1.08	0.818	0.1402	1.7	2536	23	2933	12	2977	14	13.5
c.5-3	909	6	0.01	63	0.02	0.05743	1.09	0.64	1.4	0.0806	0.88	0.629	0.0228	13.87	499.8	4.2	508	24	508	24	1.6
c.6-1-3	125	80	0.66	46.6	0	0.20821	1.2	12.46	1.81	0.4339	1.36	0.747	0.1255	2.15	2324	26	2892	20	2962	22	19.6
c.6-2	200	101	0.52	51.7	0.2	0.12329	1.09	5.0999	1.52	0.3	1.06	0.694	0.0898	1.87	1691	16	2004	19	2080	24	15.6
c.6-3	3344	140	0.04	238.1	0.06	0.05723	0.81	0.6537	0.93	0.0828	0.45	0.486	0.0241	6.03	513.1	2.2	500	18	500	18	-2.5
c.6-4	222	112	0.52	52.8	0.07	0.12413	1.02	4.75	1.5	0.2774	1.1	0.733	0.0805	2.06	1578	15	2016	18	2132	23	21.7
c.6-5	64	28	0.46	26	0.11	0.20837	1.04	13.59	1.99	0.4729	1.7	0.853	0.1478	2.67	2496	35	2893	17	2938	19	13.7
c.6-6	56	25	0.46	20.4	0.18	0.20399	1.15	11.82	1.99	0.4203	1.62	0.816	0.1034	2.81	2262	31	2858	19	2935	21	20.9
c.6-7	264	130	0.51	93.5	0.07	0.20101	0.57	11.42	1.11	0.412	0.95	0.856	0.1184	1.44	2224	18	2834	9	2915	11	21.5
c.7-1	894	8	0.01	64.7	0.06	0.05845	1.59	0.6787	1.71	0.0842	0.63	0.366	0.0375	36.96	521.2	3.1	547	35	547	35	4.7
c.7-2	549	10	0.02	38.7	0.48	0.05733	2.83	0.6469	2.97	0.0818	0.9	0.305	n.d	n.d	507.1	4.4	504	62	504	62	-0.5
c.7-3	1289	11	0.01	92.2	0.08	0.05751	1.32	0.6599	1.46	0.0832	0.62	0.426	0.0254	46.37	515.4	3.1	511	29	511	29	-0.9
c.7-4	47	21	0.46	21.7	0.13	0.21498	1.36	15.8059	2.58	0.5332	2.19	0.849	0.1536	3.51	2755	49	2943	22	2962	24	6.4
c.7-5	99	30	0.31	32.7	0	0.20146	1.47	10.6862	2	0.3847	1.35	0.677	0.1509	2.46	2098	24	2838	24	2943	27	26.1
c.7-6	218	97	0.46	90.9	0.01	0.20664	0.68	13.82	1.26	0.485	1.07	0.844	0.1335	1.51	2549	22	2879	11	2916	12	11.5
c.7-7	190	93	0.5	66.7	0	0.20596	0.64	11.59	1.23	0.408	1.05	0.854	0.1149	1.54	2206	20	2874	10	2962	13	23.2

Notes: All Pb in ratios are radiogenic component, all corrected for ^{204}Pb.
disc. = discordance, as 100 - 100{t[$^{206}Pb/^{238}U$]/t[$^{207}Pb/^{206}Pb$]}
4f^{206}Pb = (common ^{206}Pb) / (total measured ^{206}Pb) based on measured ^{204}Pb.
Uncertainties are 1σ; n.d.=not determined.
$^{207}Pb/^{206}Pb$ ages (Ma): (1) lead-loss to zero (i.e. Recent); (2) Cambrian lead-loss